ECAP-2020-016

Comparison of Directional Reconstruction Algorithms of Muons using the Moon Shadow in IceCube

Master's Thesis in Physics

Presented by

Sebastian Schindler

30 November 2020

Physikalisches Institut IV
Erlangen Centre for Astroparticle Physics
Friedrich-Alexander-Universität Erlangen-Nürnberg

1. Supervisor: Prof. Dr. Gisela Anton
2. Supervisor: Prof. Dr. Uli Katz

Contents

1. Introduction

The IceCube Neutrino Observatory is located at the south pole and traces the secondary particles from neutrino interactions using a cubic kilometer of ice instrumented with over 5000 photmuliplier tubes. It made a first detection of astrophysical neutrinos in 2013 [7]. Since then, the search for their origin has been one of the main goals of the IceCube experiment [6]. Among the secondary particles are muons that travel in nearly identical direction as the parent neutrino, and thus the reconstruction of the muon track direction allows searching for the sources of astrophysical neutrinos.

Directional reconstruction algorithms are being continuously improved. Determining the performance of these algorithms is an important task, both to judge new algorithms against existing ones, and to arrive at a good estimation of their uncertainty. This is normally done using Monte Carlo simulations, in which the true direction is known besides the reconstructed direction. Because this measure of performance is dependent on the correctness of the Monte Carlo simulations, a measure based mainly on experimental data is also desirable. In many astronomical fields of study, so-called standard candles, astronomical sources with well-known properties, are used as a means of verification of the instrument [2]. However, no known source of astrophysical neutrinos exists.

A solution is using the Moon's shadow in cosmic rays. These arrive isotropically at Earth with no traceable source either, though they are blocked by the Moon, which creates a sink in the cosmic ray flux. This translates to a sink in the atmospheric muon flux, which are muons originating from cosmic rays, and which are detected by IceCube besides neutrinos. The reconstruction of atmospheric muon tracks is similar to those originating from neutrinos. The difference is that atmospheric muons arrive in muon bundles instead of a single muon. However, this difference can be neglected in first order, which allows to use the same reconstruction algorithms as for muons from muon-neutrino; additionally, a sink can be treated similarly to a source. Thus, with the knowledge of the Moon's changing position, an effective sink in the muon flux can be observed. This sink should be clearer to resolve using a better-performing reconstruction algorithm.

A Moon analysis for observation of the Moon's cosmic ray shadow has been done before by other experiments than IceCube (for example in [1]), and by IceCube in 2013 [15] and with more data in 2019 [35]. These analyses concentrated on the observation of the Moon shadow itself, instead of using it for testing reconstruction algorithms. In

this thesis, a Moon analysis is used to compare the performance of two new reconstructions with existing ones. The first is the SegmentedSpline algorithm [34], which is an improvement on the best-performing standard reconstruction used in IceCube. The second recosntruction is a Recurrent-Neural-Network-based (RNN) algorithm that is currently in development [3]. The goal is to judge the performance of those two algorithms in comparison with existing standard reconstructions without relying solely on Monte Carlo simulations, and to compare the results with those from a traditional Monte-Carlo-based assessment as a cross check for the latter. The analysis used in this thesis is mainly based on the recently developed methods in [28].

This thesis starts by summarizing the particle physics relevant to a Moon analysis in Sec. 2, and describing its principle in more detail in Sec. 3. The creation of the data sample for the analysis, and the working principle of the individual reconstruction algorithms, is explained in Sec. 4. In Sec. 5, the analysis methods are presented, and optimized and verified in Sec. 6. Eventually, the reconstruction algorithms are compared with the results from the Moon analysis and using Monte Carlo simulations in Sec. 7. A summary of the findings is given in Sec. 8.

2. Physical basics

In this chapter, the particle physics relevant for the analysis and the IceCube detector are explained. An overview of astrophysical neutrinos as the motivational basis of a Moon analysis is given in Sec. 2.1. Cosmic rays are the source used in this analysis and are described in Sec. 2.2. This thesis deals with the direction reconstruction of muons inside the underground IceCube detector that is detailed in Sec. 2.3.

When talking about particles in this chapter (specifically neutrinos, muons and electrons), most of the time also their anti-particles are implied, with the composition of primary cosmic rays as a major exception. All interactions of particles described here happen similarly for their anti-particles.

2.1. Astrophysical neutrinos

2.1.1. Neutrinos and their sources

Neutrinos are electrically neutral leptons that come in electron, muon and tauon flavours, accompanying the three charged leptons (see Fig. 2.1) [5]. They distinguish themselves from other elementary particles by their miniscule, but non-zero, mass and their exclusive coupling to the weak force besides gravity. Due to the small interaction range of the weak force, the interaction cross section with regular matter is extremely small. Neutrinos are thus able to penetrate large amounts of matter without loosing energy or being deflected. This makes them very promising astrophysical messengers, as they always point towards their origin and are not absorbed, as opposed to photons. Several fundamental properties of neutrinos are subject of ongoing research, like the exact mass and the possible existence of more than three flavours.

The high-energy (TeV and PeV) astrophysical neutrino flux was found by IceCube [7], and an IceCube-initiated multi-messenger observation produced evidence that blazars are a source of this flux [8]. A much larger number of high-energy neutrinos are created from cosmic rays in Earth's atmosphere. These atmospheric neutrinos arrive uniformly distributed over the whole sky, with a decreasing energy spectrum starting in the GeV range and reaching up to PeVs [9]. Other neutrino sources with low energies in the keV

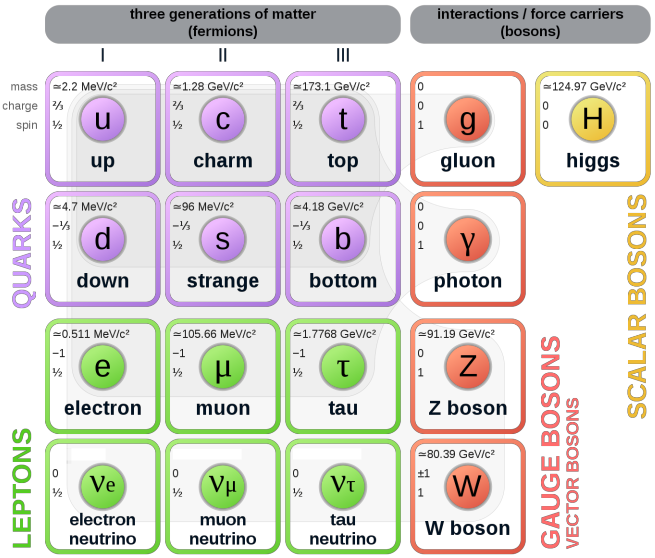

Figure 2.1: Overview of the Standard Model of particle physics. Neutrinos, the main particle of interest in IceCube, are shown in the bottom row. This thesis deals mainly with muons originating from cosmic rays, which are hadrons and consist of quarks. Adapted from [4].

and MeV range are very abundant, like terrestrial neutrinos from beta decays and from the sun's nucleosynthesis. Supernovae events in the Milky Way or another close galaxy (like SN1987A [10]) also produce low-energy neutrinos with large rates.

2.1.2. Detection principle

The detection of neutrinos requires very large detector volumes due to their small interaction cross section with matter. Because they do not couple to the electromagnetic force, direct calorimetric measurements, as they are used for charged particles, are not possible. Radiochemical methods deliver no direction information of the neutrino [11], so the detection of secondary particles from neutrino-matter interactions is used in IceCube. Deep-inelastic scattering [5] with a nucleon from the detector material is mediated either by a $W^{\pm}$ boson or a Z^0 boson for a charged (CC) or neutral current (NC), respectively (see Fig. 2.2). In both cases, the neutrino interacts with a quark, braking up the nucleon and producing a number of hadronic particles as a result. In a CC interaction, the charged lepton corresponding to the neutrino's flavour is emitted from the vertex and is detected, while in the NC case, the initial neutrino survives and produces no further detectable signal.

The resulting secondary particles are either detected directly, or first multiply in number and develop into cascades of particles that are large enough to be detected. Four general types of events can be distinguished and are shown schematically in Fig. 2.3. In all cases, a hadronic cascade is produced from the shower of hadronic particles in the interaction. If an electron is produced by a CC electron-neutrino interaction, an electromagnetic cascade develops from an interplay of Bremsstrahlung losses of the electron and subsequent

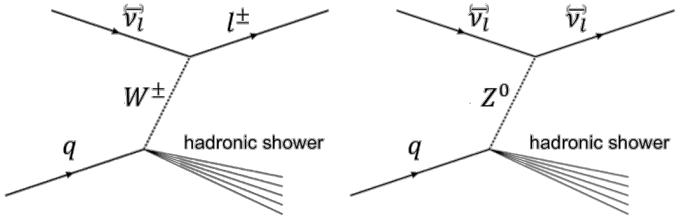

Figure 2.2.: Feynman diagrams of deep-inelastic scattering of neutrinos off a quark from a nucleon. Charged (left) and neutral current (right) interactions both produce an undetermined number of hadronic particles, but only CC interactions produce a lepton corresponding to the neutrino's flavour. The process works similarly for anti-neutrinos with a positively charged anti-lepton produced.

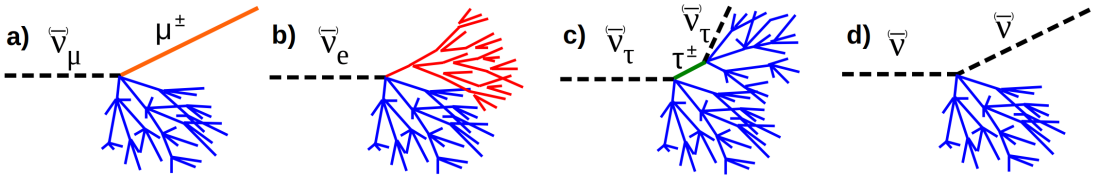

Figure 2.3.: Schematic representation of the four different neutrino event types visible in IceCube, with electromagnetic and hadronic particle cascades in red and blue, respectively. The itself unobservable neutrino enters from the left and either: a) – c) transforms into a lepton (CC) or d) leaves the detector again (NC). The produced lepton can be: a) a muon or b) an electron that develops into an electromagnetic cascade or c) a tauon that quickly decays and produces either a hadronic cascade (as shown), or a muon or an electron (similar to a) and b)). Taken from [12].

pair production from the emitted photons in the vicinity of a nucleus. A muon, produced by a muon-neutrino, travels away from the vertex along a straight track without being stopped or deflected. Tauon-neutrino CC interactions take on a signature that is similar to the muon- or electron-neutrino CC cases, or with an additional hadronic cascade, based on the decay products of the short-lived tauon.

Eventually, the secondary particles are detected via their Cherenkov light emission by many light sensors spread out across the detector volume (more details later in Sec. 2.3). Muons are observable as straight tracks through the detector, and with reconstruction algorithms, their travel direction is estimated. Because of the high energies of the neutrinos that IceCube can detect and due to Lorentz boost, the muon travels nearly parallel

to the original neutrino. Thus, the reconstructed track points towards the origin of the neutrino, which allows to search for astrophysical neutrino sources using muon tracks[1].

2.2. Cosmic rays

Cosmic rays produce atmospheric muons via air showers, which are the main background for muon-neutrino detection. In a Moon analysis, these atmospheric muons are the main signal.

2.2.1. General

Cosmic rays[2] are charged particles that originate from outside Earth and arrive isotropically distributed over the sky [20]. Compared to neutrinos, they have a very large interaction cross section with regular matter, and are thus blocked by the Earth or the Moon. The cosmic ray flux consists mainly of atomic nuclei and few electrons and antiparticles. The composition is energy-dependent, but quite constant up to energies of about 100 TeV, at (mass-wise) 74 % protons, 18 % alpha particles and a remainder of heavier nuclei [5]. At very high energies (PeVs), the fraction of the most massive nucleus ^{26}Fe can be equal or larger than the fraction of hydrogen in the flux.

The energy spectrum (see Fig. 2.4) covers 12 orders of magnitude in eV, peaking at 300 MeV and reaching 300 EeV (3×10^{20} eV). The flux drops rapidly with increasing energies to less than one particle per year and km^2, while at the smallest energies a cosmic ray intersects one m^2 every second. The energy spectrum is described by three power laws $E^{-\gamma}$ with different spectral indices γ, which produce kinks in the spectrum called the "knee" and "ankle", as the curve to some is reminiscent of a human leg. The energy range accessible to IceCube starts at about 1 TeV [15] due to threshold effects explained later. Figure 2.5 (left) shows the cosmic ray energy spectrum as it is used in this thesis.

The lowest-energy cosmic rays below IceCube's threshold originate from solar flares and higher energies from unknown galactic and extragalactic sources. Tracing them back to these sources is impossible due to their charged nature. The particles are subjected to magnetic fields permeating space during their travel towards Earth, which bends

[1] Due to neutrino oscillations – a change in the neutrino's flavour after some propagation – astrophysical sources are observable with muon-neutrinos, independent of the flavour(s) with which they are produced in the source.

[2] Specifically *primary* cosmic rays; the distinction is explained in Sec. 2.2.3.

[3] The Moon filter will be explained in detail in Sec. 4.1.1. It contains a conservative energy cut, so the energy range visible here is slightly constrained compared to all events detected by IceCube.

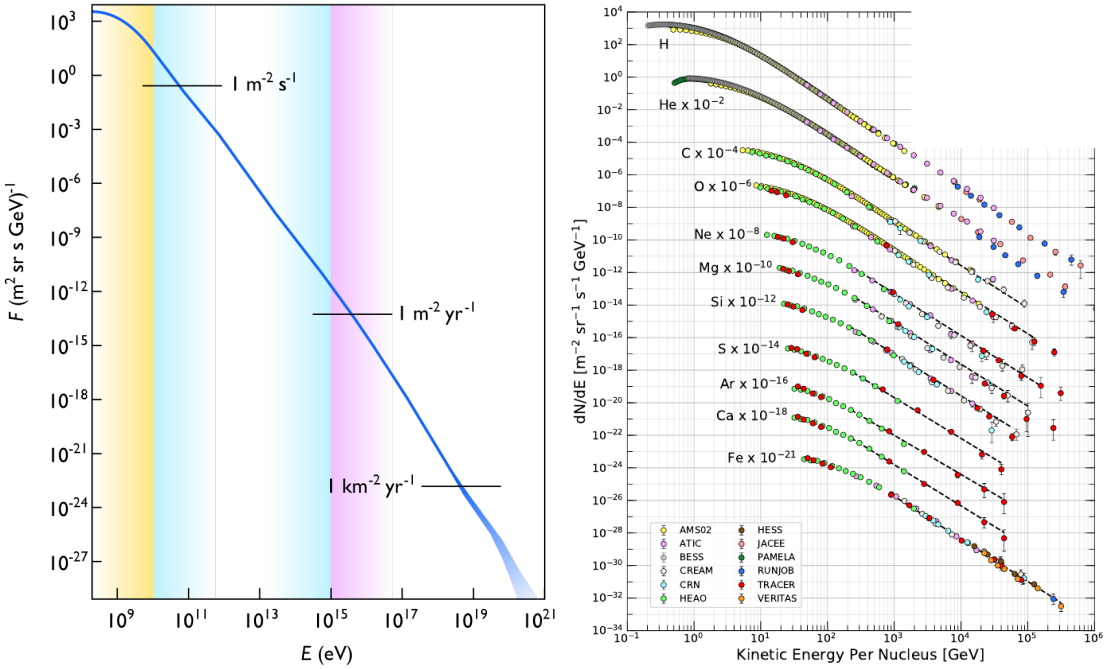

Figure 2.4.: Left: Schematic cosmic ray spectrum. Yellow, blue and red shaded regions indicate origin of cosmic rays from sun, galactic and extragalactic sources, respectively. Taken from [14]. Right: Spectrum measured by different experiments, distinguished between elements, and shown for a limited energy range. Data for different elements than H is shifted downwards. Adapted from [5].

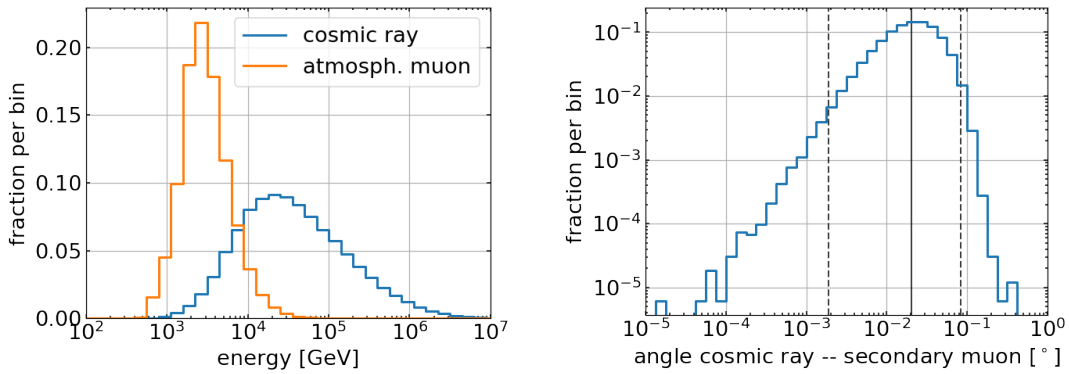

Figure 2.5.: Primary cosmic ray and resulting secondary muon from simulation data that pass the Moon filter[3]. Left: Energy spectrum for primary cosmic ray and the resulting atmospheric muon (highest-energy muon in the muon bundle). Right: Distribution of angle between them, with vertical lines marking the median and 1 % and 99 % percentile.

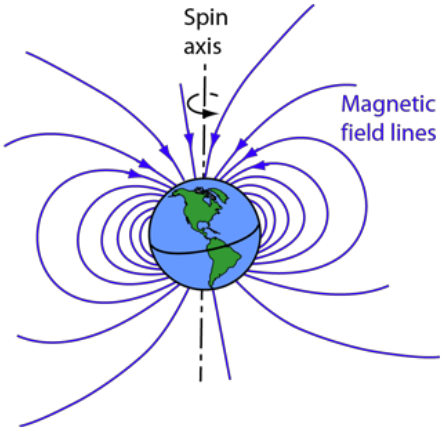

Figure 2.6: Schematic depiction of the geomagnetic field. The magnetic south pole towards which the field lines point is 11° offset from the geographic north pole. Taken from [18].

their trajectory according to the Lorentz force. This removes any directional information which the cosmic rays had after production, so that they arrive isotropically at Earth. Apart from extragalactic sources like blazars, which are believed to contribute the highest-energy portion of the cosmic ray spectrum (purple shaded in Fig. 2.4 (left)) [8], sources inside our galaxy contribute the middle energy portion (blue shaded). Such sources are for example supernovae remnants where particles undergo shock front acceleration, which deflects charged particles between two expanding shock waves of matter, increasing their energy until they are released [16].

2.2.2. Geomagnetic field

Apart from the deflection in galactic magnetic fields that cosmic rays experience, they are also deflected shortly before their detection in Earth's magnetic field. The distances over which the geomagnetic field acts is much shorter than interstellar distances, so the deflection is only small and does not make a Moon shadow observation impossible.

The geomagnetic field is approximately described by a dipole field, as it would be produced by a bar magnet that is tilted by 11° with respect to the Earth's spin axis, as illustrated in Fig. 2.6. The magnetic north pole is positioned close to the Earth south pole. Cosmic rays with a charge q travelling with velocity $\vec{v}$ in the geomagnetic field $\vec{B}$ experience the Lorentz force $\vec{F_L} = q\vec{v} \times \vec{B}$. The magnitude of the velocity is for all cosmic rays of interest near the speed of light in vacuum; only the charge and alignment with the field lines is different between cosmic rays and thus causes different deflections.

The direction of deflection is perpendicular to the motion of the particle and the magnetic field. In a coordinate system centered at the geomagnetic pole, the dipole field is rotationally symmetric. This means that for IceCube, which is located relatively close to

the geomagnetic pole, the cosmic rays are approximately deflected in the same azimuth direction, independent of their zenith angle[4].

In a previous Moon analysis with IceCube [15], the magnitude of the deflection $\Delta\lambda$ was parametrized based on simulation studies. Cosmic rays were propagated in a magnetic field modelled according to the International Geomagnetic Reference Field (IGRF) and averaged over all possible trajectories. In dependence on the cosmic ray energy E and charge Z the following relation was found[5]: $\Delta\lambda = 1.9^\circ \frac{Z}{E[\mathrm{TeV}]}$. A higher energy causes a smaller deflection, and heavier particles experience larger deflections. In particular, iron nuclei ^{26}Fe, the heaviest portion of cosmic rays, undergo a 26-times larger deflection than p^+ of the same energy.

2.2.3. Air showers

The cosmic rays discussed above are more specifically primary cosmic rays, and their resulting particles like muons are called secondary cosmic rays[6]. They are created in interactions of primaries in the atmosphere, and are the component of cosmic rays that is typically measured. Primaries normally do not reach the ground, so a direct measurement is only possible with balloons or detectors in space, like AMS-02 aboard the International Space Station [19]. Due to the small detector size, these measurements are limited to lower-energy cosmic rays, where the flux is large. The high-energy portion is only accessible via indirect measurements of the secondaries. This can be done with Imaging Air Cherenkov Telescopes that observe an air shower initiated by the cosmic ray in the atmosphere, or with water-based Cherenkov telescopes like IceCube that detect the particles from the air shower that make it to the ground.

Air showers are created by primary cosmic rays with similar particle multiplication processes as they happen after a neutrino-matter interaction. When cosmic rays enter the Earth's atmosphere, they are much more likely to interact inelastically with the nuclei of atoms in the atmosphere than to reach the ground [20]. In these interactions at heights of 10 km above ground or higher, other hadrons are released which interact similarly with other air molecules on their way downwards, and thus a hadronic cascade is generated. In these processes also short-lived pions $\pi^{\pm/0}$ are created that decay into muons (charged pions) or two photons (neutral pion). The longer-lived muons can again decay into electrons, and the photons can undergo pair creation to produce an electron/positron pair. Electrons/positrons experience Bremsstrahlung losses, which drives the electromagnetic

[4] For small zenith angles, the deflection might be different due to the different angle to the magnetic field lines. This is irrelevant in a Moon analysis, because the Moon never rises above 30° above the horizon at the south pole.

[5] Strictly valid only until 2015 due to used IGRF model restrictions.

[6] Following this definition, atmospheric neutrinos are also secondary cosmic rays. As they behave differently and are detected less often, the term will refer here to charged particles only.

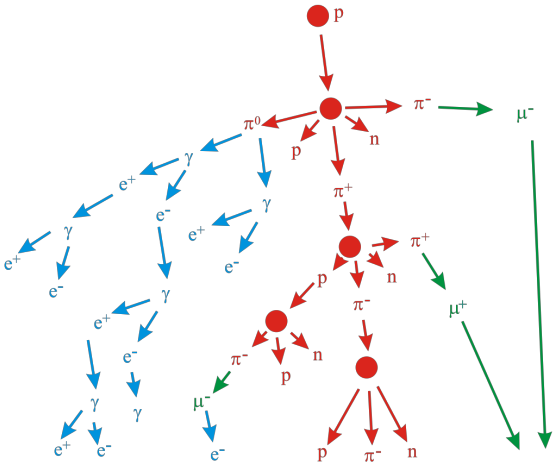

Figure 2.7: Schematic depiction of the inelastic processes happening in an extensive air shower. An incident proton (first red bullet) interacts with a molecule from the atmosphere (second red bullet), producing further particles. Hadronic processes are shown in red, electromagnetic cascades in blue and muons in green. Adapted from [21].

cascade. This results in two additional types of particle cascades besides the hadronic one: an electromagnetic and muonic shower. These processes are intertwined with each other and form an extensive air shower as shown in Fig. 2.7.

2.2.4. Atmospheric muons

Muons from air showers that reach the ground and are detected are called atmospheric muons. Muons decay with a livetime of 2.2 μs, which is longer than most other unstable particles like tauons [5]. In absolute terms, this time is still short: A quick calculation shows that a relativistic muon can travel only 660 m. However, relativistic time dilation allows muons to actually reach the ground from their creation height several km above ground.

Due to the large muon mass compared to the electron's, Bremsstrahlung losses in matter are small, which gives muons the ability to penetrate several km of material. As opposed to an air shower's electromagnetic and hadronic components, this allows atmospheric muons of sufficient energy to reach the underground IceCube detector (or for neutrino-induced muons to enter the detector from an interaction in the vicinity). This required minimum energy of an atmopsheric muon is several hundred GeV [15], which is evident from the starting point of the observed muon energy spectrum in Fig. 2.5 (left). For incident angles close to the horizon, more matter than for vertical paths, both in the atmosphere and underground, has to be penetrated for a muon to be detected. Subsequently, less muons make it into the detector and thus the atmospheric muon flux is strongly dependent on the zenith angle [20].

Atmospheric muons are an overpowering background for muon-neutrino detection, as they produce the same track signature in the detector: About 100×10^9 atmospheric

muons are detected yearly by IceCube, versus only 100×10^3 high-energy atmospheric neutrinos [13]. They can therefore only be distinguished by their orientation: Muon tracks that point downwards to horizontal are mostly atmospheric muons; horizontal to upwards travelling muons can only originate from neutrinos, because the amount of matter to penetrate is too large. For a Moon analysis, this abundance of atmospheric muons is a welcome signal.

Similar to how muons from muon-neutrinos point towards the direction of the neutrino, atmospheric muons point towards their primary cosmic ray. Muons from the same air shower arrive together in the detector as a muon bundle with nearly parallel travel directions. At the energies of TeVs relevant to IceCube, the muon bundle's direction is very similar to the primary cosmic ray's: Fig. 2.5 (right) shows the angle between cosmic ray and the highest-energy muon from the resulting bundle, as determined from simulations. The angle is smaller than 0.1° for over 99 % of events.

2.3. IceCube detector

The underground IceCube detector observes muons and other secondary particles from neutrinos, like electrons, via their Cherenkov light emission. This light is eventually converted into a readable signal by photo sensors that monitor the detector volume.

2.3.1. Cherenkov effect

Neutrino and cosmic ray energies that IceCube is interested in are large enough that secondary particles are still relativistic and move nearly with the speed of light in vacuum. In a dielectric medium like water, this gives rise to the Cherenkov effect, an emission of UV and (mainly blue) optical light [24]. Charged particles locally polarize the medium they are moving through, and the resulting dipoles emit radiation. For a sub-relativistic particle, the emission cancels out, but for a relativistic particle, the source of emission moves faster than the emitted light, and thus a net effect is observed. Analogous to a sonic boom in air, the Cherenkov light travels along a cone-shaped wavefront with the particle, under an opening angle that is determined mainly by the medium. See Fig. 2.8 for a visualization of the geometry. The intensity of Cherenkov light is very small, so the energy loss from Cherenkov emission itself is negligible.

The amount of Cherenkov photons emitted by a single charged particle is independent of the particle's energy[7]. However, charged particles produce particle cascades, which increases the number of light-emitting particles. Therefore, the overall amount of

[7] If $v \approx c$.

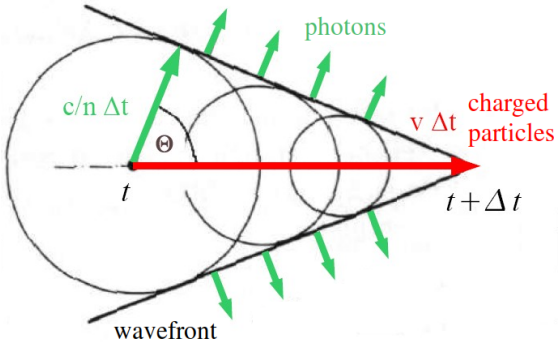

Figure 2.8: Cherenkov effect for relativistic particles in a dielectric medium. Circles indicate light emission at the position of the particle, which add up to a cone-shaped wavefront. The angle is determined by the refractive index of the medium. Adapted from [23].

Cherenkov photons depends on the energy of the initial charged particle. Muons, which do not initiate a cascade directly, and thus would emit only few Cherenkov photons, produce cascades along their track due to energy losses.

2.3.2. Muon energy loss

Many energy loss mechanisms are relevant for muons in the energy range of interest (TeVs): Primarily radiative losses from direct pair creation and Bremsstrahlung, and to a lesser extend from nuclear interactions, as well as from ionization losses. An extensive overview of muon energy loss can be found in [22]. The description of energy loss is usually split into two terms for ionization and radiative losses: $\left\langle -\frac{\mathrm{d}E}{\mathrm{d}x} \right\rangle = a(E) + b(E)E$. At the relevant energies, both $a(E)$ and $b(E)$ are only weakly dependent on E, so that the ionization energy loss is nearly constant, while the radiative losses increase linearly with energy. The critical energy, which is the point of equality between both types of losses, is for muons in water about 1 TeV [22], which is slightly larger than the smallest observed muon energy. Therefore, ionization losses are mostly the smaller component, but cannot be neglected. Direct pair production, Bremsstrahlung and nuclear interactions contribute approximately in the ratio 3:2:1.

Ionization losses happen nearly continuously, but radiative losses are more stochastic in nature. Pair production occurs most often, but the energy loss is usually small, whereas Bremsstrahlung losses can be very large when they happen. All radiative losses result in cascades: Either hadronic ones from nuclear interactions, or electromagnetic ones from a produced electron/positron pair or Bremsstrahlung photons. Therefore, additionally to the very few Cherenkov photons of the muon itself, differently sized cascades along the track contribute to the light yield of a muon. A larger energy of the muon causes – via larger energy losses due to $\left\langle -\frac{\mathrm{d}E}{\mathrm{d}x} \right\rangle \propto E$ and thus cascades with more particles – more emitted Cherenkov radiation.

2.3.3. Detector layout

Requirements for a neutrino detector using Cherenkov light are a large volume due to the small interaction cross section of neutrinos, and an optically transparent medium to transmit the Cherenkov light with no large ambient light sources. For the IceCube in-ice detector [25], an underground volume of $1\,\mathrm{km}^3$ of the glacial ice at the geographic south pole is instrumented with detector modules. These Digital Optical Modules (DOMs) each contain a downward-facing photomultiplier tube with a large diameter of 25 cm, which can convert individual photons into an electronic signal, as well as readout and calibration electronics. High-voltage and data connection is facilitated by up to 3 km long cables to the above-ground IceCube Lab control building. The detector layout can be seen in Fig. 2.9: In a hexagonal structure, 86 vertical strings are deployed with 60 DOMs evenly spaced between a depth of 1.5 km and 2.8 km. This creates a spacing of 125 m horizontally and 17 m vertically between detection units. For sensitivity to lower energies, eight strings are aligned closer together to form DeepCore. Additional water tanks with light sensors, called IceTop, are deployed at the surface to measure the electromagnetic component of cosmic ray air showers.

The in-ice detector's DOMs essentially record the number of photons and the exact time – with ns resolution [25] – at which they detected the light. Together with the position of the DOM, this gives spatial, temporal and energy resolution. Two main signatures are discernible in IceCube: Track- and cascade-like events. A detector view with examples of both signatures is visible in Fig. 2.10. The track reveals the muon's orientation and direction, and the energy can be estimated from the amount of light. The discrete emission of light due to muon energy losses is visible. A cascade signature is caused by the electromagnetic and hadronic particle cascades from electrons (or tauons decaying quickly into electrons or hadrons), and is much more symmetrical in its signature than a track.

Most muon tracks are entering and leaving the detector again, called through-going. If they originate from neutrinos, they have an interaction vertex outside the instrumented volume. Starting tracks, with a vertex inside the detector, and stopping tracks, with a muon entering the detector that happens to decay inside it, are rarer. Atmospheric muons produce only down-going tracks with at most horizontal incident angles. As only part of the muon's track is inside the detector and thus observable, the energy estimation of the primary particle (neutrino or cosmic ray) is difficult. Cascades on the other hand are very well contained in the detector volume – except if the neutrino interaction vertex happens to be at the edge of the volume –, and thus maximal information about the energy deposition is available. This allows to infer the energy of the primary neutrino with good accuracy. However, the direction information from a cascade is much less precise than from a track, so only muon-neutrinos are relevant when searching for astrophysical neutrino sources.

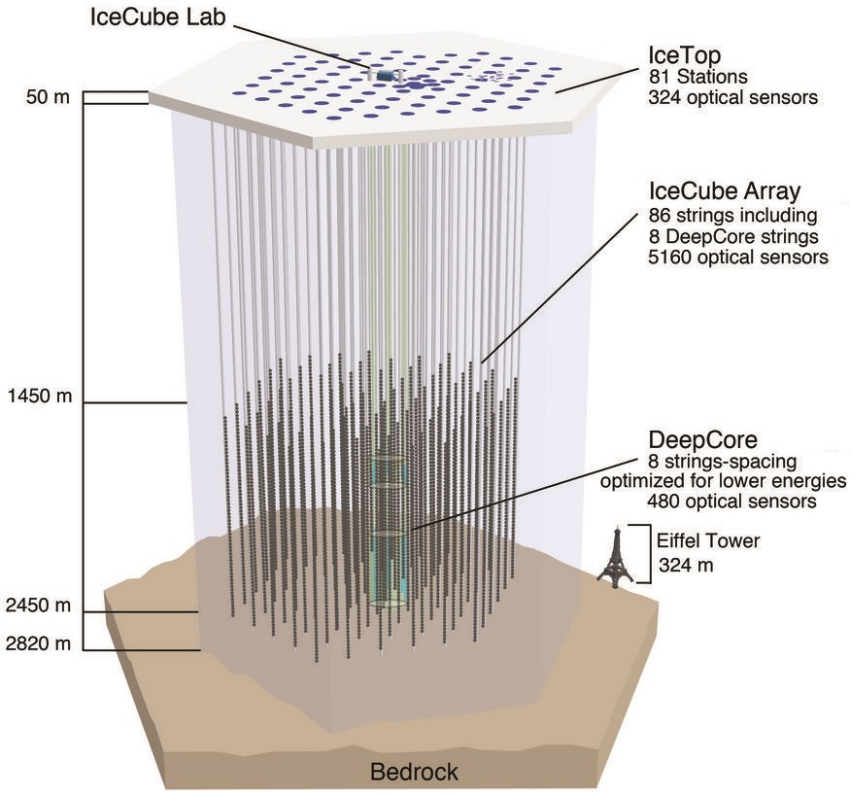

Figure 2.9.: IceCube detector with the main in-ice array, low-energy extension DeepCore, air shower surface detector IceTop and central readout and control facility IceCube Lab. The detector is built into the nearly 3 km thick glacial ice sheet at the geographic south pole.

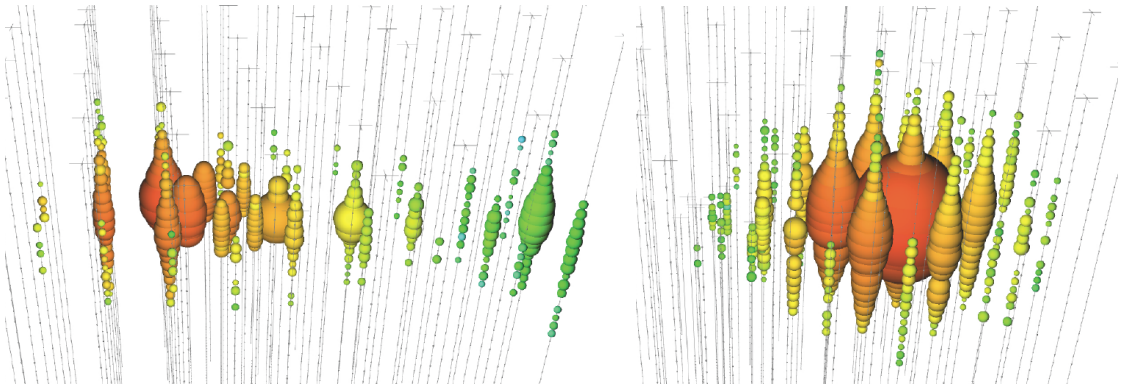

Figure 2.10.: Event view of a typical track- (left) and cascade-like event (right). Grey vertical lines with small dots are the detector strings with attached DOMs. Colored spheres indicate DOMs that detected light, with the size scaling with the amount of light and the color with the time of detection (red is earlier). Taken from [26].

3. Moon shadow analysis principle

The reconstruction of the direction of a muon track, based on the position, time and amount of light detected, is not trivial. Directional reconstruction algorithms are therefore continuously improved, which requires a quantification of their performance. This is possible by comparing reconstruction and true direction using simulations; however, in this thesis real experimental data[1] is used. To do so, a calibration source, typically called standard candle in astronomy, of muons is needed.

The only origin of muons detected in IceCube, other than neutrinos, are cosmic rays. As they arrive isotropically, there is no source of atmospheric muons either. However, cosmic rays can be blocked, and thus a sink in the cosmic ray flux can be created. As atmospheric muons retain the direction information from their primary cosmic ray, this translates to a sink in atmospheric muons. A sink in a certain baseline flux can be treated in the same way as a source above a baseline of zero, except for a minus sign. Therefore, the same general analysis methods as for a source search can be used.

The only angularly large objects, as seen from Earth, that are blocking cosmic rays are the Moon and Sun. They both have an angular diameter of roughly 0.5°, thus blocking the same portion of cosmic rays. The Sun has large and complex magnetic fields that influence cosmic rays, which complicates the analysis of a Sun shadow [35]. The Moon, however, has only a weak magnetic field [15], and therefore acts mainly as a passive blockade of cosmic rays. Being the closest astronomical object to Earth, the Moon's trajectory and therefore apparent position and size are well-studied, which makes the Moon a good muon standard candle.

On a map of the sky surrounding the Moon, the reconstructed directions from a hypothetical perfect reconstruction algorithm would show a sharp drop in the flux to zero of a Moon-sized circle – if there was no geomagnetic field. With a more realistic algorithm, the directions are smeared by a distribution that describes the algorithm's uncertainty. Subsequently, the Moon deficit will be smeared out: The deficit has no sharp edge any more, but a slope towards the center, where the deficit has a minimum that is not necessarily zero. A better-performing algorithm with a smaller uncertainty will produce a deeper minimum, as less events are erroneously reconstructed inside the Moon's disk.

[1] Simulations still have to be be used indirectly as well. Also, later the result from experimental and simulation data is compared.

Therefore, a Moon shadow analysis determines the maximum of this deficit with respect to the expected flux at this position.

The situation is complicated by the deflection of cosmic rays in the geomagnetic field. The deflection is small enough, so that it does not distort the Moon shadow as much as to be unobservable, and a shift of the shadow is also small enough to not have to look for it at a much different position on the sky [15]. Not all cosmic rays experience the same deflection, so the shadow will appear fuzzier as it would only from the smearing by the reconstruction uncertainty. Quantifying these geomagnetic effects and incorporating them into an analysis is difficult, so it is not attempted in this thesis. Instead, by applying the different algorithms to the same data, the analysis results contain the same geomagnetic effects and are thus comparable.

4. Data sample

The experimental data that is used for a Moon shadow analysis are atmospheric muon events that are reconstructed originating from the vicinity of the Moon. The production and selection of this data is detailed in Sec. 4.1. Additionally, simulation data (Sec. 4.2) is used to apply certain corrections to the data. The working principle of directional reconstruction algorithms, and specifics about the tested algorithms, are given in Sec. 4.3. Eventually, in Sec. 4.4 cross checks are performed on the data sample, to assert that the distributions of quantities, which are the input of the analysis, are well-behaved and that no unknown anomalies are present.

4.1. Event selection

It is infeasible for IceCube to permanently record the output of all DOMs all the time and use this raw data as an analysis input. Instead, a trigger system detects actual physical events and a filter system selects those worth keeping for various purposes, including a Moon analysis. Before the analysis can be performed, this data has to undergo further processing to retrieve the useful physical observables. Quality cuts are applied to reduce the amount of events that are not relevant or worsen the result. Lastly, the advanced directional reconstruction algorithms that are to be tested are applied.

4.1.1. Moon filter

IceCube's over 5000 DOMs continuously record light hits, and send charge and more detailed information about the signal and the detection time to the surface. The process of extracting the relevant information and making the decision what data to save permanently is detailed in [25]. Most hits are caused by randomly occurring dark noise, so a trigger system looks for space and time correlation of hits that originate from a physical event, such as a muon passing through the detector. If a physical origin is likely, all hits occurring during a certain time window are saved as one unit, called an event. This event undergoes a basic processing in real time at the south pole, in order to derive quick estimates of the physical observables, such as direction and energy. Now a number of filters categorize the event based on importance for different analyses, for

example, whether an event is of high energy, or whether it originates from the vicinity of the Moon. If an event is filtered, it is sent via satellite link to a data center for later use in analyses; overall about 100 GB of filtered events are sent daily.

The Moon filter is the filter of choice for this thesis. It records events based on their closeness to the Moon on the sky, and their energy. The filter is implemented since the 2011 physics run, and thus for the entire run time of the finished IceCube detector. To pass the filter, an event must be reconstructed within $\pm 10^\circ$ in the zenith coordinate of the Moon's current position, and with any azimuth. Thus, the Moon filter records a $20^\circ \times 360^\circ$ window around the Moon that is closed in azimuth and 20° wide in zenith; the majority of the events will be used for background determination. The decision of the filter is based on a fast track reconstruction algorithm, called PoleMuonLLH, which is less accurate than the advanced algorithms tested in this thesis, but more suitable for real time processing (see Sec. 4.3.2 for details about the different reconstruction algorithms). In Fig. 4.1 (left) the reconstructed direction of PoleMuonLLH relative to the Moon is shown for simulation data, together with the real direction of the same events. The zenith-dependency of the atmospheric muon flux inside the filter window is visible. By definition of the filter window, PoleMuonLLH is contained perfectly in the $\pm 10^\circ$ zenith window, but the true direction is for some events at smaller zenith angles. This is not a problem for the analysis, as no assumptions of the distribution of events inside the Moon filter window are made[1].

In order to filter out events that are not or only very imprecisely reconstructible, the Moon filter contains a minimal energy requirement. The amount of detector strings and DOMs with a recorded hit n_{string} and n_{DOM}, respectively, are proxy quantities for the energy. The filter condition of $n_{\text{string}} \geq 3$ and $n_{\text{DOM}} \geq 8$ removes only very small energy events, and is later in the processing tightened further. The last requirement of the filter is that the Moon must be above the horizon.

In local coordinates at the position of IceCube at the south pole, the Moon rises above the horizon, reaches its maximal altitude of no more than 30°, and sets again in the zenith coordinate. This happens over a period of about twelve to 14 days, and is shown by the black line in Fig. 4.2 (left). During this time, each day the Moon position performs about one revolution in the azimuth coordinate[2]. The entire trajectory traced on the sky is an upward spiral starting at the horizon that reverses and spirals downwards again. The rate of the Moon filter is defined primarily by the Moon's zenith coordinate, and thus varies significantly due to the strong zenith dependency of the atmospheric muon

[1] The zenith dependency in the filter window is not parameterized, but instead derived from data itself – see Sec. 5.1. Thus, the distribution can have any shape, and the imperfections of the filter-defining reconstruction are not a problem.

[2] The Moon's orbit around the Earth takes approximately 30 days, which is much slower than the Earth's rotation. Thus, in equatorial coordinates, the Moon moves only little each day, while the Earth rotates once, causing the Moon to cover the entire azimuth range each day for an Earth-bound observer.

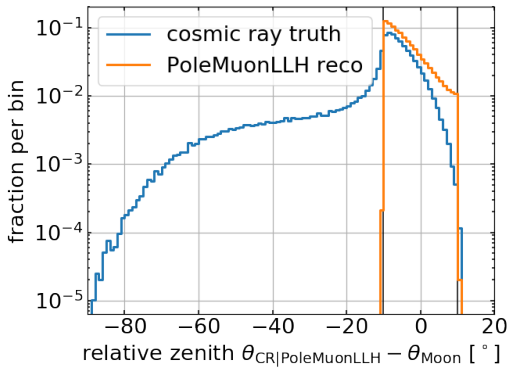

Figure 4.1: Zenith distribution of Moon filter data relative to the Moon for PoleMuonLLH reconstruction and true cosmic ray direction. The Moon filter window of ±10° around 0° is indicated by vertical bars. For negative relative zeniths, the Moon has a larger zenith than the data, which means the data is above the Moon in altitude.

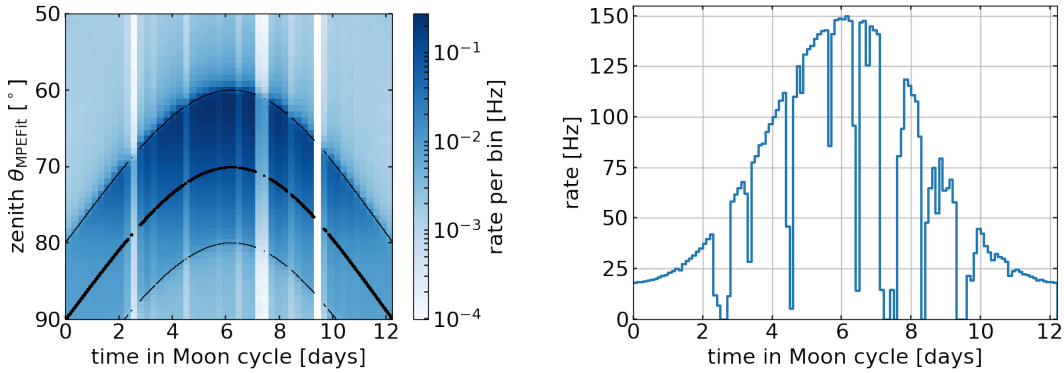

Figure 4.2.: Rate of the Moon filter as function of time in the Moon cycle, and additionally (left) as function of the reconstructed zenith. Thick black lines is the position of the Moon, narrow black lines the extends of the Moon filter. Vertical stripes in the left plot, and deviations from a smooth curve in the right plot, come from missing data due to detector downtime.

flux. The development of the rate during a Moon cycle is shown in Fig. 4.2 (right) for the Moon cycle in January 2013. The average rate during this Moon cycle is 71 Hz, which results in about 62×10^6 total events[3].

Second order effects of orbital mechanics influence the evolution of the Moon's path on the sky over several Moon cycles [27]. The largest contribution is the lunar nodal cycle, which is caused by the precession of the Moon's orbital plane. It changes with a period of 18.6 yr relative the Earth, causing the path of the Moon in local coordinates to change. This leads to a variation of the maximum altitude of the Moon in a cycle, as observed

[3]The amount of events is less than what the simple calculation of *rate times length of the Moon cycle* gives. This is due to detector downtime, during which IceCube is not recording data – see later.

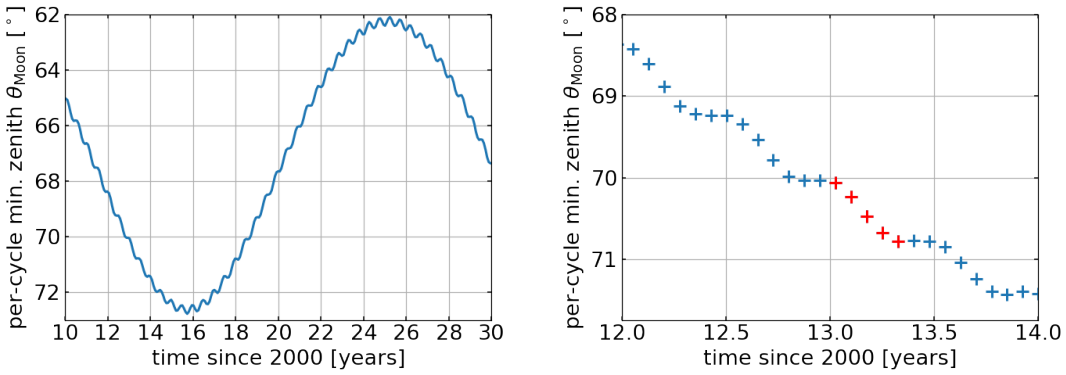

Figure 4.3.: Minimal zenith (maximal altitude) of the Moon per cycle for the years 2010 through 2030. The large periodicity of 18.6 yr is due to the Moon's nodal cycle. In this thesis, data from the first five Moon cycles in 2013, marked red in the zoom-in view on the left, are used.

from the position of IceCube. This zenith variation is up to 10° large, and its evolution over 20 years is shown in Fig. 4.3.

There are 13 Moon cycles per year. The amount of data used in the analysis is limited by the computing time required to process the data and apply the reconstruction algorithms. Because one Moon cycle already produces a large statistics, it is sufficient to use only several cycles in this thesis. IceCube is operational in its full configuration with a Moon filter since 2011, so over 100 Moon cycles of data are available. A natural choice in the context of the nodal cycle are Moon cycles with a large altitude. In this way, a single Moon cycle can have enough statistics for a Moon analysis already. The exact choice was made based on the existence of matching simulation data: The January 2013 Moon cycle was the template of an existing simulation dataset, so this Moon cycle was chosen for experimental data as well. Additionally, the following four cycles are used. In the following, these first five Moon cycles in 2013 will be referenced as "cycle 1" to "cycle 5".

One difference in rate between the cycles is the livetime, which is the time during which data is available, and which often does not cover the entire cycle. Missing livetime is visible as gaps in Fig. 4.2 (right), which varies between cycles: Some cycles have nearly 100 % livetime, while others, such as cycle 1, are without data for about 20 % of the cycle's time range. This time is also not the same for all cycles: Cycle 3 is the longest cycle, and cycles 1 and 5 the shortest, with a difference of about seven hours, or 2 %. Besides variations in actual or livetime, the nodal cycle reduces the maximum altitude from cycle 1 to 5 by less than 0.2° per cycle, causing a smaller rate. Overall, the total number of events for the five cycles are similarly large. Cycle 1 will be used throughout this thesis representative of the others, when distributions of various quantities are shown.

4.1.2. Data processing

All of the filtered data, which is sent daily to the data center, undergoes a general processing step in which a number of basic standard reconstructions are applied. For use in this analysis, the data has to undergo further processing, during which it is treated with more sophisticated methods specialized for muon tracks, and advanced reconstruction algorithms are applied. Throughout the processing chain, which consists of several steps, quality cuts are applied to the data, which are detailed in the next section (Sec. 4.1.3).

The data processing used in this thesis is based on the standard processing for muon analyses. The first step is the splitting of coincident events. Due to the large rate of atmospheric muons, about a sixth of the events passing the Moon filter actually consist of one or more overlapping events. These coincident events are separated by an involved algorithm that performs a variety of causality checks on the recorded hits. Those hits that are likely to originate from the same muon are grouped together as a new event. In the next step, random dark noise hits are removed by hit cleaning algorithms. Based on the recorded time of a hit and its position, given the finite velocity of light, some hits cannot contribute from the same muon and are thus removed. After this processing of the raw data is done, the basic standard reconstruction algorithms are repeated on the data, and more advanced energy and direction reconstruction and uncertainty estimation algorithms are run. Finally, the reconstruction algorithms that are to be tested in the analysis are applied, SegmentedSpline and the RNN-based reconstruction.

4.1.3. Quality cuts

The goal of this thesis is not to see the Moon shadow as best as possible in absolute terms, and to derive an absolute significance of the observation, but to test directional reconstructions using the Moon shadow. For this, the Moon shadow has to be discernible well from the background, but it is not necessary to fully optimize the shadow's visibility. This is normally achieved by applying quality cuts on parameters that are measures of the goodness of fit of the reconstructions. Here, only light cuts that do not remove a large portion of events are used, with the goal of testing the reconstructions also with less optimally reconstructed events and to keep the statistics high. The used cuts are meant to remove events that are so badly reconstructible, that keeping them in the data set only increases processing time for no gain.

These light cuts were found in a study by [28] and are re-used here without further investigations. To remove events with low energy, the cut on the number of DOMs that detected hits, which is also used by the Moon filter, is increased to $n_{\mathrm{DOM}} \geq 12$. Additionally, the reduced logarithmic likelihood of the standard reconstructions must

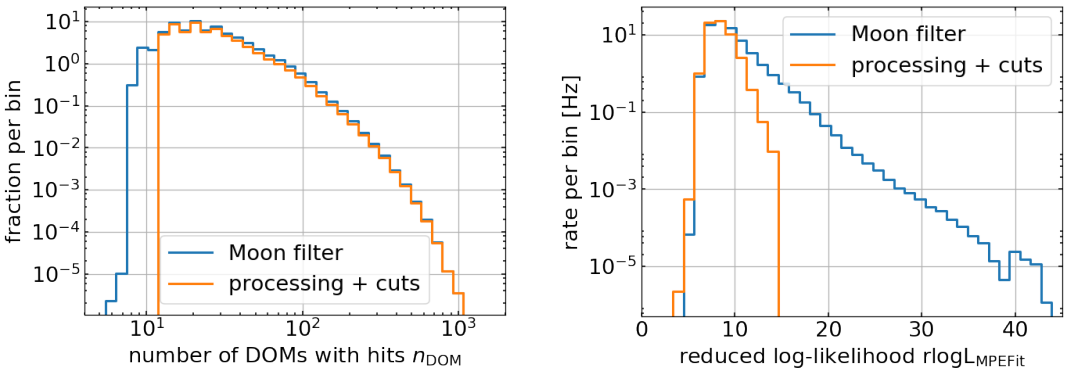

Figure 4.4.: Distributions of the number of hit DOMs n_{DOM} (left) and reduced log-likelihood rlogL (right). The blue curve is the entire data sample that passes the Moon filter, orange curve is the data after applied processing, including quality cuts. The effect of the cuts is clearly visible as a sharp drop-off. In individual bins, the curve after processing and cuts can be above the Moon filter curve, because besides applying cuts, the processing splits events and re-applies reconstructions, which can slightly change the distributions.

pass the condition rlogL < 14. This value is a measure of the success of the fit of a directional reconstruction. It is defined as the maximal logarithmic likelihood (which is negative) of the fit divided by its degrees of freedom:

$$\mathrm{rlogL} = \frac{-\log \mathcal{L}}{N_{\mathrm{dof}}}.$$

The degrees of freedom are given by[4] $N_{\mathrm{dof}} = n_{\mathrm{DOM}} - 5$ [29].

The cuts are applied at different points in the processing chain. Right at the beginning, the n_{DOM}-cut is applied before the splitting of coincident events, and repeated after the splitting, because dividing hits into several events decreases the number of hits in every single event. After these cuts, and after the reconstructions were run on the cutted events, the cut on rlogL is done for the best of the basic standard reconstructions (called MPEFit), and repeated for the even better advanced standard reconstruction (called SplineMPE; see Sec. 4.3.2 for more details about the reconstructions).

The distribution of the cutted quantities before and after the cuts are shown in Fig. 4.4. Overall, 82 % of the events survive these cuts. Before these events enter into the analysis, however, additional cuts on the uncertainty are applied. They are necessary due to more technical reasons in the analysis, and are described in Sec. 5.3.4.

[4]Five parameters define a track: one point in three dimensions and a direction.

4.1.4. Background reduction

The Moon analysis is interested in events from the vicinity of the Moon. Therefore, the data window of interest would be no larger than $20^\circ \times 20^\circ$ centered at the Moon, limited in zenith by the Moon filter specification. The filter, however, saves the entire azimuth band, and thus 17 times more data. This data is used for the background estimation, which requires larger statistics than the source region around the Moon. To save processing time, the background data is reduced to about 7 times as much data than in the source region, which is deemed sufficient for the analysis.

4.2. Monte-Carlo simulations

Monte-Carlo simulations are artificial data that mimics real experimental data as good as possible. Simulations are treated in the same way as experimental data: The same data processing, including cuts, is performed and the same reconstructions are applied. The advantage of simulation data over experimental data is the knowledge of the truth. The direction and energy of the primary cosmic ray, which is the input to the simulation production, is still known after the processing, so the reconstructions can be compared with the truth. This way of judging a reconstruction algorithm's performance is compared to the result from the Moon analysis in Sec. 7.3. Additionally, the true error from simulations are necessary to perform a pull correction on the experimental data (Sec. 4.3.3).

Cosmic rays and the resulting air showers are simulated using the CORSIKA [30] software. It simulates primary cosmic rays for all incident directions, and with an energy distribution following the phenomenological poly-gonato model [31] in the range 600 GeV to 1×10^{11} GeV. Interactions with air molecules and decays of primary and subsequent particles of the shower are simulated and all particle trajectories tracked. The particles resulting from a CORSIKA air shower are used as input for the rest of the simulation chain, which consists of simulating the Cherenkov light emission from the muons, the propagation of photons in the ice, the photo sensor's response to light, the electronics and readout system. Noise hits are added to the data and the same software triggers and filters are applied, as they run on the south pole. For the Moon filter, a Moon position is randomly drawn from cycle 1 (January 2013). This was an arbitrary choice when the simulation data was produced prior to this thesis, and determines the Moon cycle used for experimental data. Drawing Moon positions from a real cycle makes the simulations more realistic, even though the simulation of a fixed Moon at its largest altitude would result in larger statistics.

CORSIKA simulations are computationally very expensive, so the available data with properly simulated Moon filter is limited: Only around 200 000 events passing the Moon filter are contained in the simulation set. Because the real rate of atmospheric muons is large, this means that the simulation data amounts to only one hour of comparable real livetime (compared to 10 days or more livetime during a Moon cycle in experimental data). This is by far not enough data to perform the Moon analysis exclusively with simulated events as well, which would be a good test of how realistic the entire simulation chain is. However, it is enough simulation data for the necessary pull correction.

Coincident events are included in the simulation procedure, however, they cannot be used for comparisons with the true direction. As a coincident event has several primary cosmic rays, it is unclear which of those should be used for calculating the true error of an applied reconstruction. However, even if all of those events are properly splitted during the processing, due to technical reasons, the Monte Carlo truth is not available anymore after the splitting. Consequently, all coincident events must be excluded from the simulation data for purposes involving the true direction.

4.3. Directional reconstruction algorithms

Important considerations for directional reconstruction algorithms is their accuracy – both the systematic error (systematic offset from the true direction), as well as the statistical error (fluctuation of reconstructed direction), should be small – and the necessary processing time. Fast, but less accurate, reconstruction algorithms, like PoleMuonLLH, are used in real time during filtering at the south pole. For later analysis more accurate reconstructions are desirable, however their processing time must not be arbitrarily large, as this limits the analysis of large datasets. Apart from an accurate result of the reconstruction, the estimate of its statistical error must be accurate as well.

4.3.1. Uncertainty estimation

The statistical error of a directional reconstruction is an angular error in azimuth and zenith. As those coordinates are curved, the uncertainty is instead expressed in an auxiliary coordinate system that is (approximately) flat and orthogonal (further discussion can be found in Sec. 5.3.1). Even though the probability distribution of the direction can have any shape, it is often approximated by a bivariate Gaussian centered on the best-fit direction [32], as defined in (4.1). In this thesis, an asymmetric bivariate Gaussian is used, which describes the reality better than a symmetric one that is sometimes used; a difference in error between azimuth and zenith is already expected from the detector

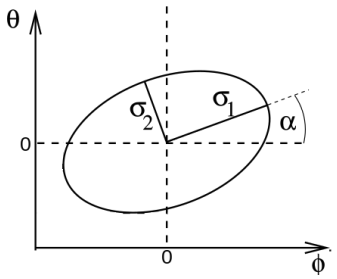

Figure 4.5.: Parametrization of the elliptical uncertainty contour. The ellipse is centered at zero in an auxiliary coordinate system with azimuth-like ϕ and zenith-like θ. The size is defined by the lengths of the semi-major axis σ_1 and semi-minor axis σ_2, and the orientation is fixed by the angle α between horizontal axis and semi-major axis.

layout, which has a finer spacing along one direction than the other. Consequently, the 1σ-contour of the uncertainty is an ellipse.

A bivariate Gaussian $f_2(\vec{x})$ centered on the origin is defined by a covariance matrix $\mathbf{\Sigma}$, which is a positive semi-definite 2×2 matrix:

$$f_2(\vec{x}; \mathbf{\Sigma}) = \frac{\exp\left(-\frac{1}{2}\,\vec{x}^{\mathrm{T}}\,\mathbf{\Sigma}^{-1}\,\vec{x}\right)}{2\pi\sqrt{\det\mathbf{\Sigma}}} \tag{4.1}$$

The two eigenvalues of the covariance matrix give the squared lengths of the semi-major and semi-minor axes of the elliptical 1σ-contour, called σ_1 and σ_2, respectively. To parameterize an ellipse centered on the origin fully, a third information describing the orientation is necessary: The angle α between horizontal coordinate axis and the semi-major axis, which is calculated from the orientation of the larger of the two eigenvectors. Fig. 4.5 shows a schematic of the ellipse parameterization.

4.3.2. Overview of algorithms

A directional reconstruction algorithm derives the muon track, defined by a direction and position, from the time, position and charge of the observed hits. Most algorithms use a maximum likelihood method to find the best-fitting track parameters. The description of the likelihood contains the probability distribution of the arrival times of Cherenkov photons at the DOMs [34] for a given track. A better-performing reconstruction algorithm typically uses a more accurate description of this probability. In the data processing, reconstructions are run after each other with increasing performance. The result of a lower-performance reconstruction is used as the first guess, called seed, of the next one, which together forms a seeding chain.

Basic reconstructions

The first algorithm to start the seeding chain is a simple line fit to the position of the hit DOMs in the order of their hit times. Several algorithms follow in the seeding chain, up to the multi-photo-electron fit, called MPEFit, the best-performing of the basic algorithms. It uses in its arrival time distributions only the first photon detected by each DOM, because on average the first photon is impacted less by non-realistic assumptions of the ice properties, like scattering of photons. The PoleMuonLLH reconstruction, which is used for online processing, performs slightly worse than MPEFit. These basic reconstructions have the advantage of short processing times, however their accuracy is worst of all reconstructions: The median error of MPEFit in the data sample (after processing and quality cuts), as determined from simulations, is 1.87°.

SplineMPE and Paraboloid

The last directional reconstruction of the standard algorithms in the seeding chain is SplineMPE, which is used as the baseline for comparison with the new reconstructions. The main improvement over MPEFit is the use of a realistic ice model. The glacial ice of the detector medium is not homogeneous, which impacts photon propagation and therefore the arrival time distributions at the DOMs. The ice properties are modelled from experimental studies, and the resulting arrival time distributions are recorded for many simulated track realizations. This data is fitted by so-called B-splines, which leads to the name SplineMPE [34]. The most important remaining simplification used by the algorithm is the assumption of a continuous energy loss of the muon along the track. To compensate for this, further empirical improvements are implemented in SplineMPE, called *SplineMPE with maximal settings*. In this thesis, only the maximal settings are used, and for simplicity are referred to just as SplineMPE. With a median error of 1.35°, SplineMPE has a lower error than MPEFit.

SplineMPE itself does not give an estimate of its uncertainty. Instead, a dedicated algorithm called Paraboloid [32] derives this estimate for a maximum likelihood reconstruction like SplineMPE. The bivariate Gaussian that describes the uncertainty becomes a two-dimensional parabola – a paraboloid – in the logarithmic likelihood space around the best-fit direction. The algorithm places a grid in a flat auxiliary coordinate system around the specified seed, in this case SplineMPE. Per grid point, the likelihood is optimized by varying the vertex position, which together with the direction describes a track. Afterwards a paraboloid is fitted to the evaluated grid, which then defines the elliptical 1σ-contour. The majority of the data processing time, excluding the time for the two new reconstructions, is spend on Paraboloid with an average of approximately 3.8 s per event.

SegmentedSpline

The most obvious shortcoming of the SplineMPE reconstruction is the assumption of a continuous muon energy loss along the track. SegmentedSpline [34] addresses this issue, by placing a number of cascades on points along the track, which models the actual energy loss pattern from the dominant radiative processes: These type of interactions are very stochastic processes of large, sudden energy losses, which produce cascades of particles. Additionally, SegmentedSpline uses a noise term per DOM that represents dark noise, and has an option for an added continuous energy loss, as used by SplineMPE solely.

The input hypothesis is a seed track, in this case the SplineMPE result, and additionally a spacing of cascades along the seed, for which a value of 10 m is selected, leading to about 100 cascades. The reconstructions happens in two steps. First, only the energy of the cascades is fitted and then fixed for the second step. There, again B-splines are used to find the photon arrival time distributions, which are now also produced from the light of the cascades, instead of only a continuous light emission as for SplineMPE. As the likelihood maximization becomes a > 100-dimensional problem due to the cascades, the processing time on average reaches 21 s per event. The median error of $1.39°$ is larger than for SplineMPE. However, this must not be taken as a meaningful comparison, as simulations are used to arrive at this number, which also have only a small statistics, and because the number is an average over all energies.

An uncertainty estimation is directly included in the SegmentedSpline algorithm by analytically computing the Hessian matrix from the B-splines used in the direction fit [34]. The inverse Hessian gives the covariance matrix, which defines the bivariate Gaussian and thus the elliptical 1σ-contour. This method improves on Paraboloid by not using a finite grid for the evaluation of a likelihood, which can lead to instabilities, and it is also faster. Alternatively, an uncertainty estimation with a Markov Chain Monte Carlo method is possible that samples the likelihood space. This is a computationally expensive process, and due to the already large processing time per event, it is not used in this thesis.

RNN reconstruction

The RNN-based reconstruction algorithm uses a recurrent neural network, and thus a completely different concept from the other algorithms. It is trained on single muon events for the reconstruction of muons from muon-neutrinos. As the Moon data consists of muon bundles, the RNN reconstruction is not optimized for use with a Moon analysis.

The uncertainty estimate is only a symmetrical Gaussian, so circular uncertainty contours are used instead of elliptical ones.

An advantage of the RNN reconstruction is its fast processing time of 0.1 s to 0.2 s per event. The median error as determined from simulations is 1.27°.

4.3.3. Uncertainty scaling

The meaning of the 1σ-contour from an uncertainty estimate is the following: The probability that the true direction lies within the contour is 39 %[5]. Consequently, for the entire data set, 39 % of events should have their true direction lie within their respective 1σ-contour. However, for all three uncertainty estimators (Paraboloid, SegmentedSpline and RNN reconstruction), this is not the case, and the portion is smaller than 39 %. This means that overall, the uncertainties are overestimated, and the 1σ-contours should be larger than they are. This is a known systematic problem, which can be rectified by a scaling of the uncertainties, called pull correction.

The pull is defined as the true error, which is the angular distance between the directions of reconstruction and truth, divided by the 1σ-uncertainty estimate:

$$\text{pull} = \frac{|\vec{x}_{\text{reco}} - \vec{x}_{\text{truth}}|}{\sigma}.$$

For the elliptical uncertainty contours of Paraboloid and SegmentedSpline, the quadratic mean of the length of the two ellipse axes is used instead:

$$\sigma = \sqrt{\frac{\sigma_1^2 + \sigma_2^2}{2}}. \tag{4.2}$$

As the true direction is needed to calculate the pull, it can only be calculated for simulation data. The containment of 50 % in a symmetrical bivariate Gaussian is inside a radius of 1.177σ. Therefore, the median of the pull distribution is expected to be at 1.177 for a perfect uncertainty estimate, and a correction factor of median(pull)/1.177 has to be applied to all σ. For elliptical contours, both σ_1 and σ_2 receive the same correction, so that the entire ellipse is scaled in size by the correction. Applying a correction derived from an averaged, symmetric uncertainty to an asymmetric uncertainty is a simplification. However, performing an uncertainty scaling in two directions is an involved procedure that raises additional problems that have to be solved. Such a scaling is done for the first time in [28], but for this thesis, the traditional approach is used.

Instead of calculating a single correction factor from the median of the entire sample, the correction is done energy-dependent. An energy proxy is binned and the median of the pull calculated for each bin. The pull as function of the energy proxy, shown in Fig. 4.6 (left), is fitted by a polynomial of 5th order. To correct the uncertainty estimate of any

[5] For a (one-dimensional) Gaussian 68 % of the area under the curve is contained within $[-\sigma, \sigma]$, which becomes 39 % for a bivariate (two-dimensional) Gaussian.

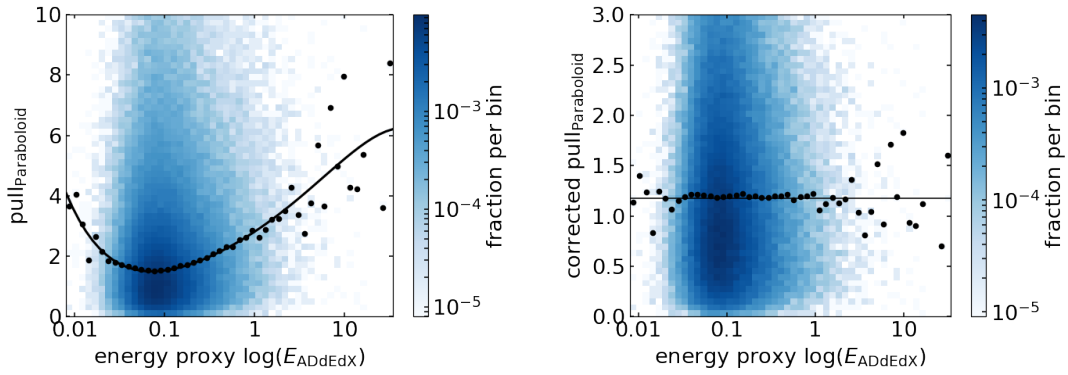

Figure 4.6.: Distribution of pull, defined as true error divided by 1σ-uncertainty estimate, and energy proxy (an energy loss estimator called ADdEdX) for the Paraboloid uncertainty estimator. Black dots are the median pull for each energy bin, to which a 5th-order polynomial was fitted. The pull correction was applied to the shown data on the right. The horizontal line indicates a pull of 1.177, along which all median pull values should line up in case of a perfect pull correction.

given event, the σ_i are multiplied by the value of the polynomial at this event's energy proxy and divided by 1.177. As a check, this is done for the same data used for the calculation of the pull correction, which aligns the median pull values more horizontally and shifts them closer to the target of 1.177, as can be seen in Fig. 4.6 (right). In the region of high statistics, they fit well to the horizontal, however at lower and larger energies, the deviation is large. This is likely due to the small statistics in the available simulation data set, but the pull correction still improves the uncertainties noticeably. This is similarly true for SegmentedSpline and the RNN reconstruction, which can be seen in the appendix in Fig. A.1 and Fig. A.2.

Another caveat besides low statistics is the exclusion of all coincident events from the simulation data. On real data, coincident events that cannot be splitted correctly during processing would lead to large errors, as two events from different directions are mixed. The exclusion of those from the pull correction could introduce a systematic error into the pull correction factor.

4.4. Cross checks

Before the analysis is performed, the data sample is checked for any unexpected behaviour. Distributions of the observables that enter into the analysis are examined and

judged, whether the visible features are expected. The distributions shown here are for Moon cycle 1. Most histograms are normalized, and contain approximately 51×10^6 events – except for quantities from the SegmentedSpline reconstruction (zenith, azimuth and uncertainty), for which only about half as many events are available (due to the background reduction). Comparisons between cycles are discussed further in Sec. 6.3 and cross checks are shown in Sec. B.

4.4.1. Data processing and cuts

First, the influence of the quality cuts and data processing is checked. In Fig. 4.7, the reconstructed directions are shown for the pure Moon filter sample ("filter data") and for applied processing and cuts. Only basic reconstructions are available on the unprocessed data, so MPEFit as the best basic reconstruction is used for this purpose.

The zenith distribution is shown relative to the Moon, so that the Moon filter window is visible. As expected, most events are contained in the window. Outside of it, the processed data favors negative relative zeniths and therefore zeniths smaller than the Moon. The filter data is approximately equally distributed between larger and smaller zeniths. This difference can have many reasons that do not have to be investigated in detail. For example, the cuts could be targeting more events close to the horizon due to some dependency on the detector geometry or the different energy thresholds for muons arriving from different zenith angles. Additionally, the more sophisticated hit cleaning and event splitting procedures during the processing could be responsible for an increase of events reconstructed at higher zeniths.

Due to the quality cuts, the amount of events in the processed data is overall smaller than the filter data. This is visible well in the azimuth distribution, and could be the reason that the amount of processed data inside the Moon window in the zenith distribution is smaller than the filter data.

The absolute azimuth distribution displays several periodic features. Most prominently, the data is six-fold periodic in azimuth. This is an effect from the hexagonal detector geometry: As can be seen in Fig. 2.9, the geometry is six-fold periodic, which means that the detector looks (in first order) the same after a rotation by 60° in the horizontal plane. Plotting the reconstructed azimuth relative to the Moon, averages over these features and creates a flat distribution.

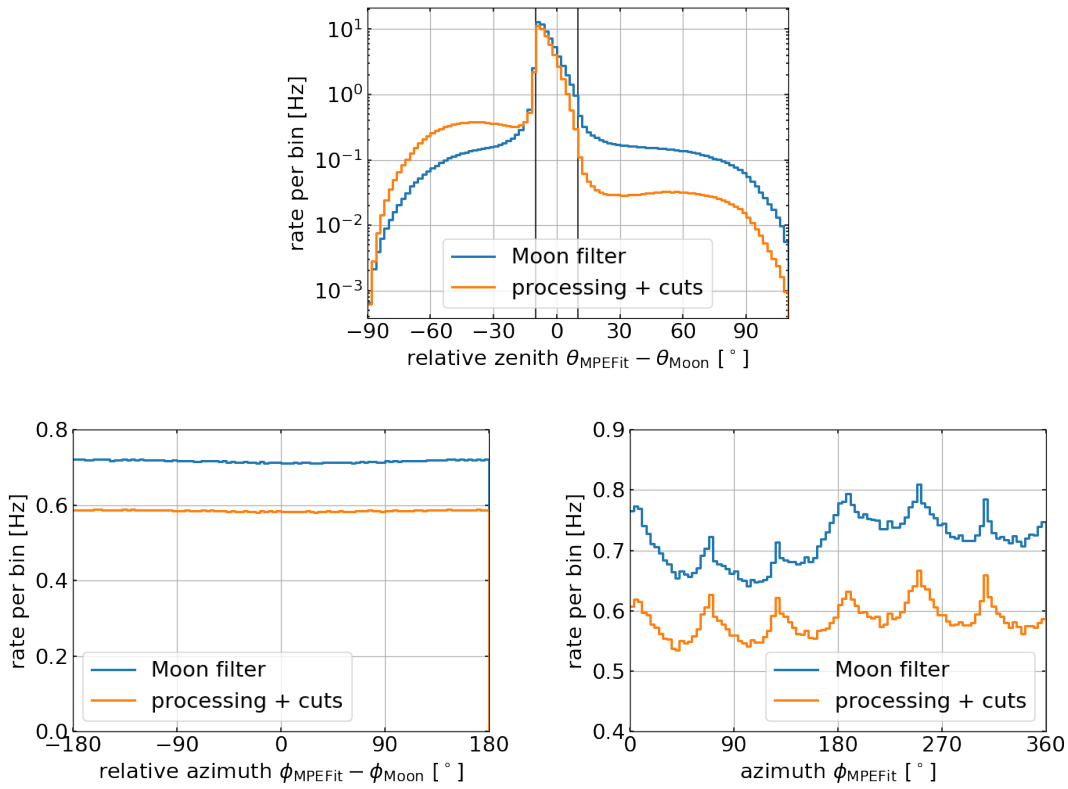

Figure 4.7.: Reconstructed direction distributions before (blue) and after (orange curve) quality cuts and processing. Top: zenith relative to the Moon, bottom: azimuth relative to Moon (left) and absolute (right). Shown are the reconstructed directions from the MPEFit algorithm. Vertical black bars in the distribution in zenith indicate the Moon filter window.

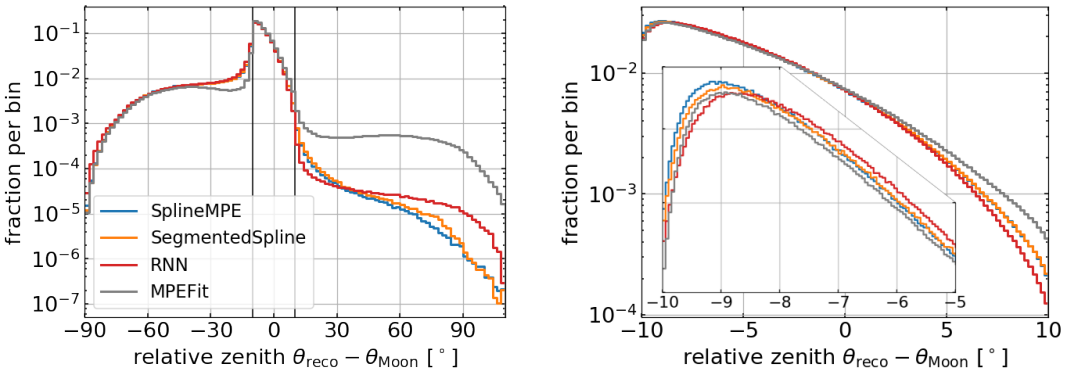

Figure 4.8.: Zenith distribution of the three advanced reconstruction algorithms SplineMPE, SegmentedSpline and RNN reconstruction. For comparison, the best basic reconstruction MPEFit is shown in grey. The distribution inside the Moon window (left) is normalized with respect to the shown data range, and thus the overall larger rate of MPEFit inside the window is not visible there. The inset shows a zoom on the peak of the distribution. At large relative zeniths inside the Moon window, SplineMPE and SegmentedSpline overlap.

4.4.2. Comparison of reconstructions

On the processed and cutted data, the different reconstructions can be checked against each other. The zenith distributions of the three advanced reconstructions, and MPEFit for comparison, are shown in Fig. 4.8. All three advanced algorithms behave similarly, with differences only visible in regions of low statistics, and MPEFit behaves visibly different to them. More than MPEFit, all three favor smaller zeniths than the Moon, which indicates a systematic tendency of the former. Inside the Moon window, MPEFit has the largest portion of events of all reconstructions. The reason is that MPEFit is closer in nature to PoleMuonLLH, which defines the filter window, and thus agrees better with the Moon window than the other reconstructions.

The distributions inside the Moon window are very smooth due to the large statistics. This is necessary, because the Moon is only a small deficit, and too large fluctuations can hide this deficit. The Moon deficit itself is not visible in the distribution, because it contains data from the entire azimuth band: Many million events are contained in the histograms, however, the number of events shadowed by the Moon are on the order of hundreds up to a thousand.

For the three advanced reconstructions, the uncertainty estimate can be compared as well. Fig. 4.9 shows that overall SegmentedSpline has the smallest uncertainty estimate

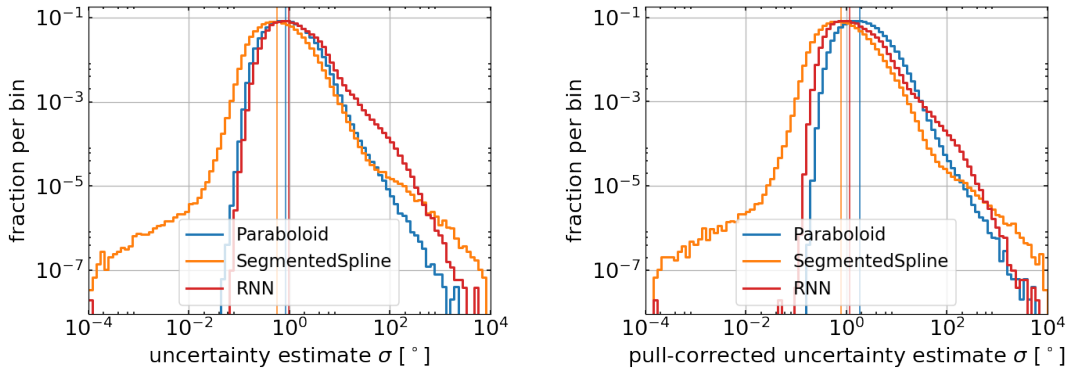

Figure 4.9.: Uncertainty estimate from the three advanced algorithms. For Paraboloid and SegmentedSpline, the symmetric uncertainty calculated from the asymmetric estimates is shown. The uncertainties with applied pull correction are shown in the left. Vertical bars show the median uncertainty.

of the three. After pull correction, the uncertainty of RNN is the next largest. This might indicate the performance of the reconstructions already; however, the pull correction is not error-free, so this should be taken with caution.

5. Analysis methods

Previous work on Moon shadow observations with IceCube used several different approaches to the analysis. General considerations for a Moon analysis, and the choice of the analysis type, are detailed in Sec. 5.1. A simple analysis that allows to see a Moon shadow is presented in Sec. 5.2. In Sec. 5.3, the more sophisticated method that is mainly used for this thesis is explained in detail.

5.1. Design choices

The main goal of the analysis is to measure the depth of the Moon shadow, because this is a measure for the accuracy of the reconstruction. Additionally, the shadow center's position and its size and shape, influenced primarily by geomagnetic effects, are of interest to judge the validity of the shadow depth. It is not sufficient to simply create a histogram of the area surrounding the Moon: In Fig. 5.1 data from all five Moon cycles is taken together, and only a very faint shadow is observable after normalizing in zenith. The strong zenith dependency of the atmospheric muon flux makes a deficit superimposed on this dependency difficult to observe. To overcome this problem, the zenith dependency has to be subtracted from the data around the Moon, called the source window. For this, an estimate of the background distribution is needed, which contains the overall zenith dependency in the data, without a shadowing effect by the Moon.

Background estimation

Because the Moon filter saves the entire azimuth band, the data sample contains data from all azimuths at the same zenith as the Moon, for each Moon position in zenith. As the Moon covers the entire azimuth range several times, coordinates relative to the Moon also contain at each point contributions from all azimuths. Consequently, all relative-azimuth regions away from the source window are good background estimates, as they are averaged in azimuth and zenith in the same way the source window is. Worded differently: Due to the Moon occupying all azimuth positions several times in

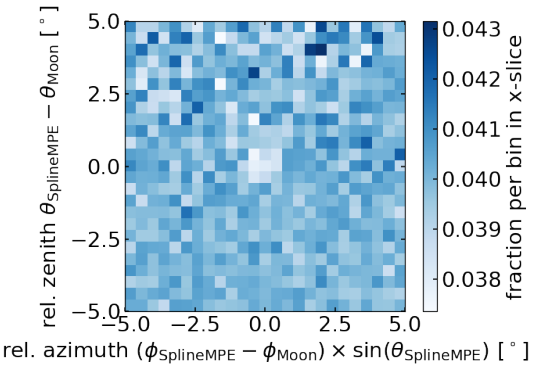

Figure 5.1.: Distribution of events in the region surrounding the Moon. Five Moon cycles of data are used with 2.3×10^6 events in the shown area. To counteract the zenith dependency, each slice of bins in azimuth (bins that have the same zenith), is normalized independently from the others. The azimuth coordinate of each event is multiplied by the sine of the zenith to correct for the non-orthogonality of the azimuth coordinate.

the sample, coordinates relative to the Moon are averaged over all azimuths and therefore flat, and thus all regions away from the source window are a good background estimate.

For the source window, only few degrees in azimuth and zenith around the Moon are needed for the analysis. Due to the limited size in zenith, the source window will not be larger than $20° \times 20°$ around the Moon. This leaves 340° in azimuth to spare for the background estimation. From this region, several background windows of the same size as the source window are taken, and stacked on top of each other. The amount of background data is thus larger than the data in the source window, which limits fluctuations in the background estimation. This is important, because the significance of the Moon shadow is computed from the deficit in the source window compared to the background window.

Analysis designs

The exact method of the comparison between source and background is what distinguishes different analyses. A one-dimensional analysis makes use of the radial symmetry of the problem: The Moon is an extended spherical source[1], so in spherical coordinates centered at the Moon one can restrict the analysis to a profile view. Source and background are compared only in dependence of the distance to the Moon, integrated over the

[1] Actually, the Moon is a sink in a finite flux, and not a source above zero. As this difference amounts to only a sign – a sink can be viewed as a negative source –, the word source will be used for simplicity here.

angle. In a two-dimensional analysis, a landscape of the source-background difference is evaluated around the Moon position. This allows for finding the position of the deficit, as well as observing the shape. The comparison can be done by creating a histogram and comparing individual bins, or in an unbinned way by using a maximum likelihood method.

The first Moon analysis with IceCube was performed with data from the unfinished detector in 2013 [15]. It used a binned 1D analysis and a simple unbinned 2D analysis. The latter used symmetrical uncertainty estimates in the likelihood description and a background estimation that only encoded the zenith dependency. With data from the finished IceCube detector, another Moon (and Sun) analysis was done in 2019 [35], using the same binned 1D analysis, and a binned 2D analysis. Recently, the unbinned 2D analysis, used in the first publication, was improved in several ways by Saskia Philippen [28], including the use of asymmetric (elliptical) uncertainty estimates, a better background description and source model. In this thesis, the binned 1D analysis is performed as a first check whether the shadow is observable, and the improved unbinned 2D analysis is used to arrive at the main results.

5.2. Binned 1D analysis

The same binned 1D analysis as in [15] is used here, and therefore only a short overview is given.

In the on-source window, and eight off-source windows that are distributed over the azimuth range, the angular distances from the center are calculated. The on-source window is centered on the Moon, and the off-source windows are centered at the same zenith at another azimuth. Histograms are created for each window with the same binning.

Now, the relative shadowing for the i-th bin is calculated as follows:

$$\frac{N_i^{\mathrm{on}} - \left\langle N_i^{\mathrm{off}} \right\rangle}{\left\langle N_i^{\mathrm{off}} \right\rangle}. \tag{5.1}$$

N_i^{on} is the number of events in the i-th bin in the on-source window, and $\left\langle N_i^{\mathrm{off}} \right\rangle$ is the number of events in the i-th bin of each off-source window averaged. A Poisson error can be propagated from the bin contents to the relative shadowing.

5.3. Unbinned 2D analysis

The task of a Moon analysis is similar to a neutrino point source analysis: Finding the significance of existence and position of a source. Thus, a similar ansatz for the analysis design can be used: A search on a grid around an expected position, using the maximum likelihood method. The two-dimensional unbinned maximum-likelihood analysis used here is heavily based on the improved version developed recently by Saskia Philippen. More details about the methods as well as verifications can be found in [28].

There are several advantages of the unbinned 2D analysis over a binned 1D analysis. The two-dimensional landscape gives information about the position and shape of the shadow, which is lost in a 1D profile view. The source window is not histogrammed, which avoids problems arising from the selection of the bin size. This unbinned method also allows to take into account the uncertainty estimate, which is a piece of information not usable by a binned method. The background estimate can be determined in a binned or unbinned way. Lastly, a more realistic disk source model is used, instead of the simplification of a point source used for an extended source like the Moon.

5.3.1. Coordinate system

The result of a directional reconstruction is a point on a sphere that is described by an azimuth and zenith coordinate. This is a problem, because the analysis requires flat, orthogonal coordinates, and azimuth and zenith are not orthogonal for zeniths different than 90°. As the 1D analysis only uses distances to the Moon, calculating the angular distance was sufficient. For the 2D analysis, many points around the Moon have to be addressable, and thus, a proper coordinate system has to be defined. This is done by transforming to a system that is approximately orthogonal around the Moon. Most reconstruction algorithms already internally use such a coordinate transformation to an auxiliary system, perform the fit procedure there, and reverse the transformation afterwards. An exception are the uncertainty estimators, which do not perform the reverse transformation, so strictly speaking, the uncertainty contour is only valid in an orthogonal coordinate system.

On the equator, azimuth and zenith are orthogonal (equi-azimuth lines are parallel), so a transformation to an orthogonal system is done by a rotation to zenith 90° and azimuth 0°. This point is the origin of the coordinate system that is here called equator system[2]. It is approximately planar, with a maximum deviation of 0.15 % for distances less than 5° from the origin [32]. The analysis will incorporate events reconstructed farther than 5° away from the Moon, however, the most important region is closer than that. The

[2]Not to be confused with the equatorial system, the standard geocentric astronomical coordinate system.

coordinates in the equator system should be called azimuth-like and zenith-like, instead of azimuth and zenith, as they are strictly speaking not azimuth and zenith anymore. However, for simplicity, they will be called *relative azimuth* and *relative zenith*, even though they are not the same as the difference between reconstruction and moon in both coordinates, which would normally be called *relative*.

Direction reconstruction algorithms rotate the given seed track to the origin of the equator system, and apply the reverse rotation to the finished reconstructed direction. For the analysis, the Moon is rotated to the equator system origin, and thus, all directions in the vicinity of the Moon are now expressed in orthogonal coordinates relative to the Moon. This is done at first for the source window only, as the orthogonality holds only for small distances from the origin. The background events are transformed only after they are shifted to smaller distances from the Moon, which will be explained in 5.3.4.

5.3.2. Maximum likelihood method

The maximum likelihood method is already employed in the individual reconstruction algorithms, which derive the direction from the DOM hits. Now, this method is used in the analysis to derive the Moon shadow from all of those directions. In a maximum likelihood procedure, parameters are varied for some assumed hypothesis. Here, the hypothesis is a Moon shadow at a certain position, and the varied parameter is the number of events blocked by the Moon, relative to the expectation without Moon. For a source, the normal procedure is to vary the parameter n_{signal} that is the number of events originating from a source, thus events that are above a background. The same likelihood formulation as for a neutrino source search [36] is used here, so the parameter n_{signal} becomes negative, as a deficit from the Moon shadow is a number of events below the background. The likelihood per event is defined as:

$$L(n_{\text{signal}}; \vec{x}_i, \mathbf{\Sigma}_i) = \frac{n_{\text{signal}}}{N} \mathcal{S}(\vec{x}_i, \mathbf{\Sigma}_i) + \left(1 - \frac{n_{\text{signal}}}{N}\right) \mathcal{B}(\vec{x}_i). \tag{5.2}$$

The two main components are the probability distributions $\mathcal{S}(\vec{x}_i, \mathbf{\Sigma}_i)$ and $\mathcal{B}(\vec{x}_i)$ for the i-th event to be a source or background event, respectively, which are different for each event in the ensemble of N total events. An event is defined by its reconstructed direction $\vec{x}_i$ and uncertainty estimate via the covariance matrix $\mathbf{\Sigma}_i$. The entire likelihood is a product over the likelihoods of all events; or alternatively, the entire likelihood's logarithm is the sum of the logarithms of the likelihoods of all events:

$$\log \mathcal{L}(n_{\text{signal}}; \vec{x}_1, ..., \vec{x}_N, \mathbf{\Sigma}_1, ..., \mathbf{\Sigma}_N) = \sum_{i=1}^{N} \log L(n_{\text{signal}}; \vec{x}_i, \mathbf{\Sigma}_i). \tag{5.3}$$

The background distribution $\mathcal{B}$ is discussed in Sec. 5.3.4.

Source model

An event is described by a bivariate Gaussian with a shape defined by the uncertainty estimate, positioned at the reconstructed direction. The source distribution $\mathcal{S}$ can be given by the evaluation at the hypothesized Moon position of the bivariate Gaussian of this event. This simple source description is the point source model. Here, a disk source model is used: Instead of evaluating the bivariate Gaussian at the point of the source, it is integrated over the extend of the source:

$$\mathcal{S}(\vec{x}_i, \mathbf{\Sigma}_i) = \frac{1}{\pi R^2} \int_{-\infty}^{\infty} \mathrm{d}\phi \int_{-\infty}^{\infty} \mathrm{d}\theta \, \Theta(\phi^2 + \theta^2 < R^2) \, f_2(\vec{x}_i, \mathbf{\Sigma}_i) \tag{5.4}$$

The theta function $\Theta(\phi^2+\theta^2 < R^2)$ limits the integration to the disk of the Moon with a radius of R. The coordinates in the equator system ϕ and θ are the horizontal/azimuth-like and vertical/zenith-like coordinates, respectively. The Moon radius is a fixed value that is set before the analysis to 0.25°, which is a typical apparent radius of the Moon (see Sec. 6.1.2 for a discussion).

The integration necessary for the disk source model would be easiest, if carried out in spherical coordinates based on the hypothesized Moon position. However, Cartesian coordinates are used due to an already existing implementation. In the original implementation by [28], no coordinate transformation into an orthogonal system was done. Instead, coordinates relative to the Moon were used, and a correction of the relative azimuth values by the sine of the zenith applied, to retain angular distances. However, this lead to a non-circular problem for the integration, as the Moon disk was stretched to an ellipse by the correction. This integral could not be solved analytically, so a numeric integration was implemented, which contributes the largest part of the computation time for the analysis. For simplicity, the finished implementation, with removed sine correction, was re-used here, instead of developing an implementation with a more efficient integration in spherical coordinates.

5.3.3. Evaluation on grid

The likelihood method formulated above gives the likelihood for a source (moon shadow) at a certain hypothesized position. Due to the geomagnetic field that moves the Moon position, a landscape of the likelihood is determined. For each point in a grid of 160×160 points, extending $\pm 3°$ in both azimuth and zenith centered at the expected Moon position, the hypothesis is tested that the Moon is positioned there. This grid, shown schematically in Fig. 5.2, covers an area of $6° \times 6°$, resulting in a distance between grid points of 0.0375°. Compared to the Moon diameter of about 0.5°, this constitutes a fine grid. The size of the extent of the grid was choosen such that it accomodates the expected size of the observable Moon shadow, as it was found in a previous Moon analysis [15]. To test the hypothesis of a Moon positioned at any point in the grid, the

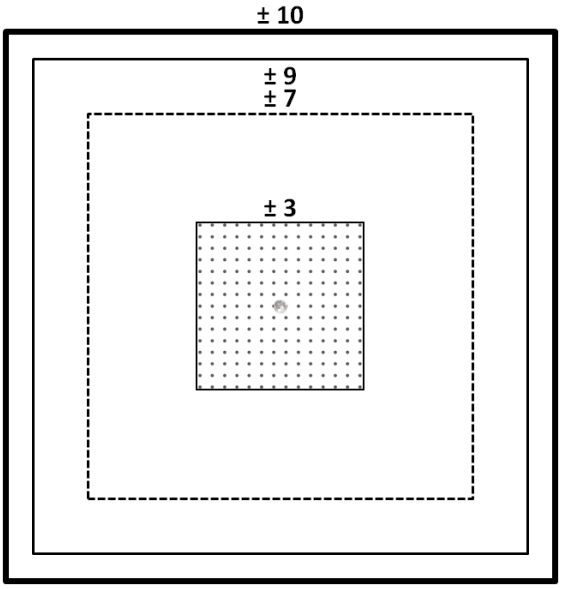

Figure 5.2: Schematic representation of the grid on which the likelihood is evaluated and the surrounding regions. The innermost box is the extend of the grid, the outermost box the maximal size of the source window. Data contributes to the grid from within the middle two (solid or dashed) boxes (see text later for further explanations). The shown numbers are distances in degrees from the center point (the expected Moon position and equator system origin) in both directions; for example, the inner grid has a size of $6° \times 6°$. Distances, including Moon size, are to scale, except for the distances between grid points.

likelihood, as formulated above, is maximized by varying n_{signal} independently for each point.

Performing this many ($160^2 = 25600$) likelihood maximizations would traditionally require very large processing times [38]. However, as the evaluation at different grid points only differs in the point of evaluation, and not the used data, this task is very well parallelizable. Graphics Processing Units (GPUs) are specialized processors designed for calculation of many similar tasks in parallel, which is originally used to accelerate a computer's video output. Increasingly, GPUs are used for scientific computing [39] and will also be used here to accelerate the evaluation. This reduces the time necessary for the analysis of one Moon cycle worth of data to several hours, or up to one day[3].

Edge effects

The Gaussian source description means that at each grid point, all events from the source window contribute to the likelihood. As a result, edge effects will be observable, if the events are only taken from the same area as the grid. To illustrate this, consider a grid point in the center of the grid, and assume that only events from within this grid are

[3]The GPU analysis uses the Nvidia CUDA software framework. Analysis times on general-purpose-computing-oriented Nvidia Tesla K20 or K80 GPU model takes several hours to complete; on an Nvidia Tesla P4 about a day or more; on a consumer-grade Nvidia RTX 2080 Ti about half a day.

used in the analysis. Events are contributing to the point's likelihood from all directions up to a distance of 3° (in a square). Now, consider a point at the center of the edge of the grid: Only half of the events can contribute in a similar way to this point as to the center point, and the other half contributes less, because they are farther away and due to the event's Gaussian description.

This asymmetry between different positions on the grid can be addressed by letting additional events from outside the grid area contribute to the grid. This larger window of events allowed to contribute to the grid is called data window, and is shown in Fig. 5.2 as the solid and dashed middle two boxes (both are used, depending on the background description detailed in the next section). However, this solution is not yet complete, because there is still an asymmetry between center and edge points: The additional events from outside the grid also contribute to the center and not only the edge point (a center point has events from the same maximal distance in all directions, while an edge point has less events available on one side, but more on the other).

The overall solution is to limit the contribution from farther-away events, which can be achieved with a cut on the uncertainty estimate. This essentially leads to an artificially limited range around a grid point, inside of which events can contribute significantly to the grid point. This cut is tailored such that this contribution range is maximally as large as the extend of the additional area beyond the grid.

The 3σ-point of the (symmetric) bivariate Gaussian of an event with an uncertainty of $\sigma = 1°$ is reached after a distance of 3° from the event's reconstruction. Beyond this point, only 1.1 % of the probability[4] is contained in the (two-dimensional) tail of the Gaussian. This is estimated to be a small enough contribution as to be negligible. Therefore, with a cut on $\sigma < 1°$, the data window around the grid window must be 3° larger in all directions. No detailed investigations into this choice were undertaken; however, it is a very similar choice as in [28], where useful results were achieved. As the uncertainty estimate is asymmetric, the cut must be applied to the semi-major axis of the uncertainty contour. The exact cut value, and therefore data window size, depends on the background model used, as will be discussed in the following.

5.3.4. Background determination

To achieve a precise estimation of the background, all available data in the azimuth band beyond the source window is used for the background estimation. The source window of ±10° around the Moon leaves free an azimuth range of 340°, which can be evenly cut into 20°-wide square windows. This results in 17 windows; however, due to the background

[4] For a bivariate Gaussian, the well-known 68.3 % – 95.5 % – 99.7 % rule becomes 39.4 % – 86.5 % – 98.9 %.

reduction that was necessary in the data processing (see Sec. 4.1.4), only about seven times as much events are contained in the background than in the source window.

To form a single square window that can be compared to the source window, the 17 background windows are each shifted until they are centered at zero, which also stacks the windows on top of each other. The coordinate transformation to the equator system is done only after the windows were shifted, because then all background events are within $\pm 10^\circ$ of the Moon (in a square).

Two-dimensional histogram

From the background window, a normalized two-dimensional histogram with 80×80 bins is created. The background estimation is not needed at the position of the grid, where the likelihood is evaluated, but it is needed at the position of each event that contributes to the likelihood. To provide a better estimate for events that are not at the center of a background bin, the histogram is interpolated between bins. The bin size cannot be decreased easily, and thus the histogram cannot be made finer, because the statistics is limited in the low-zenith region.

To avoid empty bins, the outer 1° of the background window is cut away, and the histogram determined only for the inner $\pm 9^\circ$. With this, a background estimate is available for 6° farther out from the inner $\pm 3^\circ$ of the grid window, and so the necessary cut on the uncertainty to avoid edge effects is $\sigma < 2^\circ$ (if the tolerance of 3σ is used, as discussed in the previous section).

Alternative method with uncertainty estimate

Another method for the background determination has been called quasi kernel density estimation by [28]. It incorporates the uncertainty information from background events to achieve a smoother background estimation. Instead of counting the number of events reconstructed inside the extend of a bin, the bivariate Gaussians of all events are evaluated and added up at each bin's position. The resulting landscape is again normalized and interpolated. An advantage of this method is that a smooth landscape, without any empty bins, can be retrieved from a small statistics, or likewise that a larger grid (of 160×160 points) than for the histogram method can be used.

A disadvantage is that, similar to the source window, edge effects are relevant for the background window as well, because events can contribute at a point different from their reconstruction. Subsequently, the size of the background window has to be decreased to have a larger area from where events can contribute. The stacking of regions around the origin is now as follows: The inner grid window of $\pm 3^\circ$; the data window from where

source events contribute to the grid, and where the background estimation is needed; and an additional window, from where background events contribute to the data window. The outer window can use the entire available data up to $\pm 10^\circ$, and the data window must be decreased to $\pm 7^\circ$ (for histogram method: $\pm 9^\circ$). This is the dashed box in Fig. 5.2. Additionally, the uncertainty cut has to be tightened to $\sigma < 1^\circ$ (histogram: $\sigma < 2^\circ$).

An additional caveat is the statistical correctness of this method. The background estimate is needed at the reconstructed directions of the source events, and therefore it should give the distribution of the reconstructed directions. Adding the uncertainty estimate to the background description changes that. If the statistics is very large and the uncertainty estimates are correct, this method should deliver the same result as a 2D histogram. However, the pull correction is not perfect, and thus the uncertainties are not always correct. As the available statistics is large such that a histogram gives a smooth enough estimation, the histogram method will be used primarily. The results from both methods are compared in Sec. 6.1.1.

5.3.5. Interpretation of results

The result of the unbinned 2D analysis is a landscape of the maximized log-likelihood values $\log \mathcal{L}$, and the optimal n_{signal} that causes this maximization, in an area of $6^\circ \times 6^\circ$ around the Moon. The $\log \mathcal{L}$ at each grid point is a measure for the agreement with the disk source hypothesis at this point; n_{signal} is the number of events that would be missing (negative) or arrive additionally to the background (positive) due to a Moon located at this point. An additional result is the single log-likelihood value that describes the background: $\log \mathcal{L}(n_{\text{signal}} = 0)$. If only the background is present, then $n_{\text{signal}} = 0$, and the likelihood of each event as described by (5.2) only depends on the background probability $\mathcal{B}$, and consequently so does $\log \mathcal{L}$ via (5.3).

$\log \mathcal{L}$ values itself are not very descriptive, so the landscape is examined relative to another fixed value of $\log \mathcal{L}$: The maximum of the landscape, or the background log-likelihood $\log \mathcal{L}(n_{\text{signal}} = 0)$. The difference between $\log \mathcal{L}$ at a grid point and the reference is called delta-log-likelihood $\Delta \log \mathcal{L}$.

Fig. 5.3 (top) displays the landscapes of $\Delta \log \mathcal{L}$ and n_{signal} of the SplineMPE reconstruction. The fine, but discrete, grid of 160×160 points is interpolated for displaying of a smooth landscape. In both plots, an extended deficit with its minimum roughly in the center is visible. With a size of $1 - 2^\circ$, this deficit is much larger than the Moon that has a diameter of 0.5°. The likelihood of a Moon shadow at a given position decreases with increasing distance to the most-likely position at the minimum of $\Delta \log \mathcal{L}$. Surrounding the shadow are random fluctuations above and below the background. They never reach the $\Delta \log \mathcal{L}$ of the most-likely Moon position, and in n_{signal}, they never shadow nor add

more events than the most-likely Moon position shadows. Of the two quantities, only n_{signal} has, via its sign, information about whether the likelihood at a grid point denotes a deficit or an excess.

Statistical significance

The delta-log-likelihood $\Delta \log \mathcal{L}$ is still not a very meaningful quantity on its own, and so it is used to calculate a statistical significance that allows better interpretation of the result. Following [28], two significances are derived. The source significance is the significance of observing a deviation from the background, which is split via its sign into a significance for a source above the background, or a sink below it. The second significance is the pointing significance, which describes the observation of a source or sink at the most-likely position. It gives the pointing accuracy of the reconstruction.

A likelihood ratio test is used to derive those significances. The test statistic is defined as follows:

$$TS = -2\frac{\mathcal{L}_{H_0}}{\mathcal{L}_{H_1}} = 2\left(\log \mathcal{L}_{H_1} - \log \mathcal{L}_{H_0}\right). \tag{5.5}$$

The alternative hypothesis H_1 is the observation at a grid point, and $\log \mathcal{L}_{H_0}$ is the log-likelihood of the null hypothesis, depending on the type of significance. According to Wilk's theorem [37], the test statistic TS is distributed the same as a χ^2_k distribution with k degrees of freedom. Thus, the p-value that describes the significance of the deviation between H_1 and H_0 is the survival function $1 - \text{CDF}$ evaluated at TS, where CDF denotes the cumulative distribution function of χ^2_k. The p-value is converted to multiples of the width σ of a normal distribution[5].

The two significance landscapes derived in this way are shown in Fig. 5.3 (middle), with their respective contours in a closer region around the Moon shown below.

The null hypothesis of the **source significance** is the observation of only background: $\log \mathcal{L}_{H_0} = \log \mathcal{L}(n_{\text{signal}} = 0)$. Background is determined by fixing one parameter ($n_{\text{signal}} = 0$), so the degrees of freedom are $k = 1$. The knowledge about whether a deficit or excess was found at a grid point, given by the sign of n_{signal}, is encoded in the sign of the significance: Negative significances denote an over-fluctuation, as the objective of a Moon shadow analysis is finding the deficit from the Moon.

For the **pointing significance**, the null hypothesis is the existence of a source (or sink) at the position of the $\Delta \log \mathcal{L}$ minimum: $\log \mathcal{L}_{H_0} = \log \mathcal{L}(n_{\text{signal,min}})$. The position of the source, described by two coordinates, is tested, and thus the degrees of freedom are

[5] The inverse of the survival function of the normal distribution, evaluated at half of the p-value, gives the significance in multiples of σ.

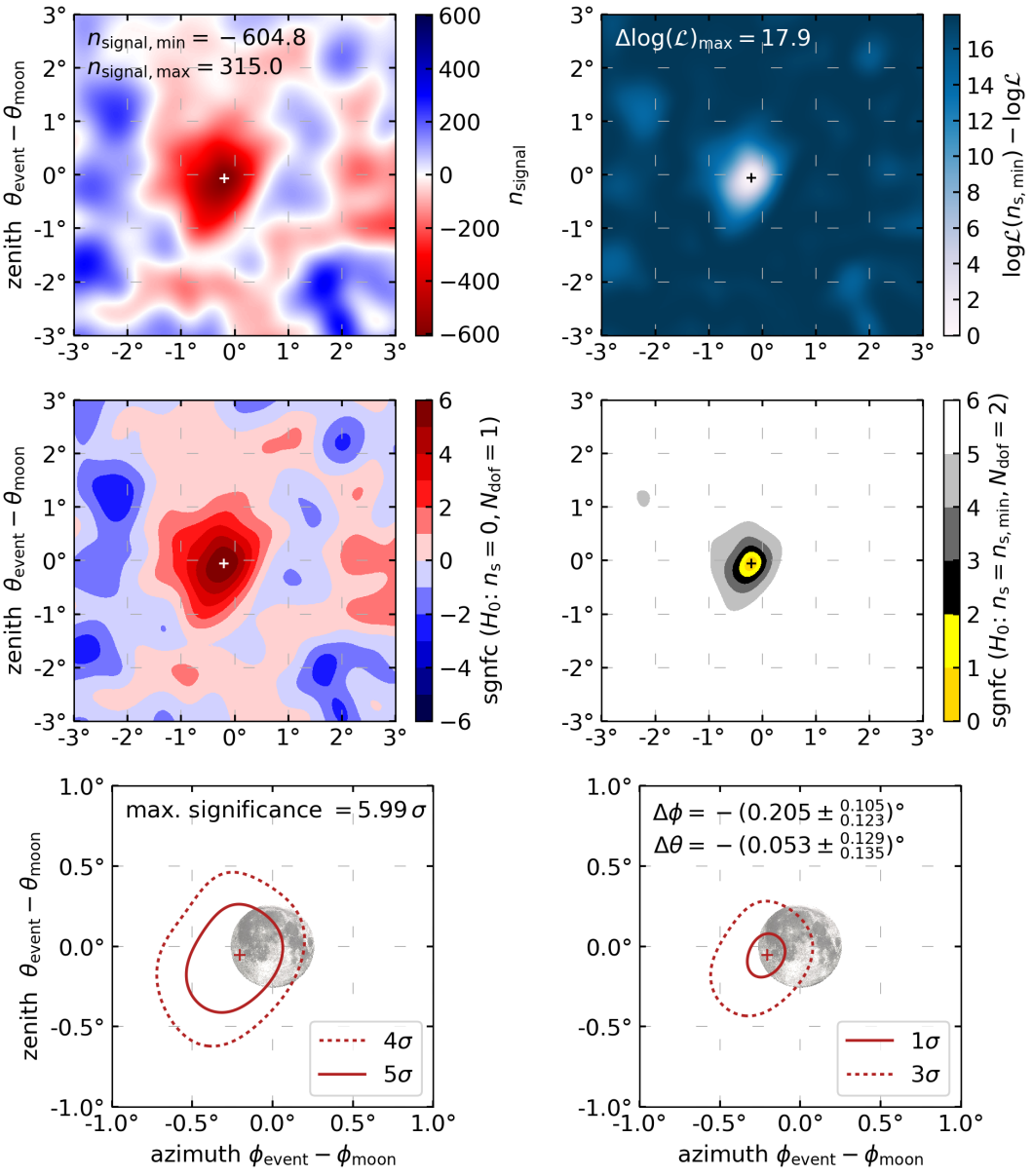

Figure 5.3.: Unbinned 2D analysis results for cycle 1, using the SplineMPE reconstruction. Top: Landscapes of the raw n_{signal} and $\Delta \log \mathcal{L}$, which is the log-likelihood relative to its maximum. Middle: Significance landscapes derived from the raw data (left: source significance, right: pointing significance). Bottom: Zoom on inner region around Moon with contours of above significance plots. The Moon shown in the center has the same size (diameter 0.5°) as used for the disk source hypothesis. Values for the maximum significance and its position at the cross marking are given.

$k = 2$. The contours of the landscape describe the probability that the source is located inside of it.

It is important to note that these significances are pre-trial values. By searching for the Moon shadow at many grid points, a trial factor needs to be included. How this factor is calculated in this case is unclear, but it is not important for the objective of comparing reconstructions. The pre-trial significances can be compared with each other, but they have only limited absolute meaning.

The final result of the analysis can be expressed as two values: The maximum of the source significance landscape, and its position including error, which is given by the extend of the pointing 1σ-contour. Additionally, the landscape contains less easily quantifiable information, like the shape of the shadow, or the significance of surrounding fluctuations, which is relevant in comparison with the maximum source significance.

6. Initial investigations

Before the Moon analysis is used to compare reconstruction algorithms, several tests are performed, using the Moon analysis' maximum source significance as an indicator for the best and desirable result. At first, in Sec. 6.1, settings of the analysis itself must be optimized, and in Sec. 6.2, settings of the reconstruction algorithms are tested. The five Moon cycles of the processed data sample are compared in Sec. 6.3, and eventually the correctness of the pull correction is verified in Sec. 6.4.

6.1. Optimization of analysis settings

6.1.1. Background model

Two background models were presented in Sec. 5.3.4: A two-dimensional histogram and the method of quasi kernel density estimation (qKDE). To determine which method to use throughout this thesis, two analyses are run with both methods and otherwise identical settings on the same data, and the maximum source significance compared.

Performing the same analysis of which the result was shown in Fig. 5.3 with the qKDE method, gives a larger significance of 6.45σ. The significance landscape is shown in Fig. 6.1 (left). To avoid edge effects, an uncertainty cut of 1° was used for the qKDE method, as it was discussed previously. With this, however, the results of qKDE and histogram method cannot be compared directly, as they use a different data sample. As the qKDE cut cannot be relaxed to the one used by the histogram method, or else edge effects would surface, the histogram method's cut is tightened instead. The result, on the right, is now comparable with the left plot in Fig. 6.1. The significance is with 6.23σ slightly less than for the qKDE method.

The stricter cut of 1° costs, compared to a 2°-cut, 44 % of the events in the source window. Using less events in the analysis generally leads to a reduction in significance; however, as the quality of the data sample rises from the stricter cut, the significance also does. For the use in this thesis, a softer uncertainty cut is preferred, in order to also test the reconstructions with less optimal events.

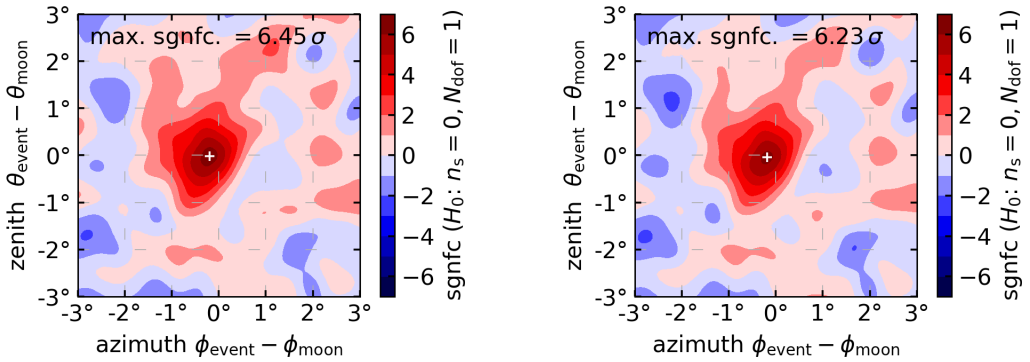

Figure 6.1.: Source significance landscape for cycle 1 with the SplineMPE reconstruction, using the quasi kernel density estimate method for the background model (left) and histogram method (right). The uncertainty is cut to 1°.

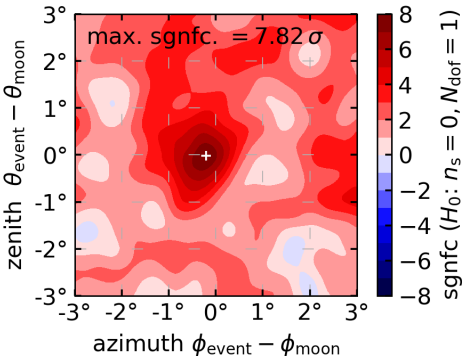

Figure 6.2: Source significance landscape for cycle 1 with the SplineMPE reconstruction, using the quasi kernel density estimate method for the background model. The uncertainty is cut to 3°, which causes edge effects that surface as an overall increase in significance.

To judge the impact of edge effects, the qKDE method was tested with higher uncertainty cuts. An increase in the cut lead to an increase in the significance, however the landscape behaved unexpectedly: The significance at all points increased, including over-fluctuations, instead of a deepening of the shadow. This can be seen for a cut of 3° in Fig. 6.2.

It is assumed that this effect comes from edge effects in the background determination. However, even without further investigations into its exact origin, it is clear that this effect is not from a physical origin, but artificial, and must be suppressed. This rules out using the qKDE method with any cuts softer than 1°, so to meet the preference of a softer cut and for simplicity, the histogram method is used. It is not a problem that the maximum significance is slightly smaller for the histogram method than for the qKDE method, because for this thesis, a reliable method for background determination is more important than one that maximizes the significance.

Table 6.1.: Maximum source significance for different Moon radius assumptions. Shows is cycle 1 in SplineMPE.

Moon radius R	0.24°	0.25°	0.26°	0.27°	0.28°	0.29°
max. source significance	5.99σ	5.99σ	5.98σ	5.98σ	5.97σ	5.97σ

In the following, the histogram background method is used always.

6.1.2. Moon radius assumption

The disk source hypothesis used as source model in the likelihood analysis must integrate over the Moon disk. The apparent Moon radius is given as a fixed parameter to the analysis, so that for all events the Moon disk has the same size. In reality, however, the apparent Moon size changes during a Moon cycle, and therefore a better description of reality would be a variable Moon radius based on the actual Moon size at the time of the detected event.

If no such variable Moon radius would be implemented, there would still need to be one fixed radius. To optimize this decision, the influence of the Moon radius parameter was tested first. From the distance between Earth and Moon retrieved from [40], the apparent radius was calculated[1]. The typical Moon distances (in 2013) between 357 000 km and 407 000 km translate to apparent Moon radii from 0.279° to 0.245°. Several analyses were run with Moon radii from this range, shown in Tab. 6.1.

The maximum source significances vary only by minuscule amounts and the landscapes (not shown) are essentially the same. Subsequently, no variable Moon radius was implemented, and the parameter fixed for all following analyses at 0.25°.

6.2. Algorithm-specific investigations

6.2.1. SegmentedSpline settings

The SegmentedSpline's cascade hypothesis models muon energy loss better than the assumption of a continuous energy loss along the track, as it is used by SplineMPE. The SegmentedSpline algorithm has a continuous loss as an option additionally to the cascade hypothesis. The largest portion of muon energy loss are radiative processes

[1] A small angle approximation is justified: $\tan\alpha \approx \alpha$.

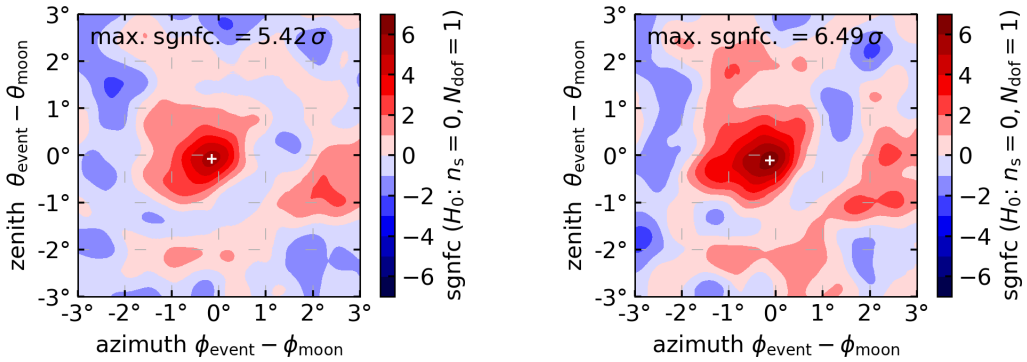

Figure 6.3.: Source significance landscape for cycle 1 with the SegmentedSpline reconstruction in the setting without (left) and with (right) additional continuous energy loss hypothesis.

that are modeled well with cascades along the track. However, for the limited energies of atmospheric muons in the Moon sample, ionization losses are not negligible. These happen less stochastically, and are better modeled by a continuous loss.

The entire cycle 1 data sample was processed for SegmentedSpline once with, and once without, the continuous loss option. The results are shown in Fig. 6.3.

The continuous loss option leads to a result with substantially better maximum significance than without it. This is expected, and thus the continuous loss option was used for all SegmentedSpline data shown in the following.

6.2.2. Uncertainty ellipse orientation

Reconstruction algorithms use an auxiliary coordinate system for the fit, which for directional reconstructions is hidden from the user, because the resulting track is transformed backwards into the ordinary coordinates. In the analysis, this track is again transformed into the equator system in which the analysis happens. For uncertainty algorithms, the result is not a direction, but an extended contour. It is not back-transformed, but instead the contour is only defined in the used auxiliary coordinate system. This makes it necessary to understand the definition of an uncertainty algorithm's coordinate system, and therefore this definition is tested here.

Uncertainty algorithms use a flat, orthogonal system, which the equator system that is used here is. However, the exact definition can deviate in the orientation of the coordinate axes, and can thus influence the orientation angle of the uncertainty ellipse.

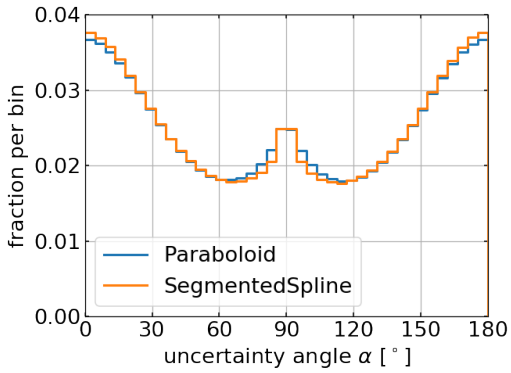

Figure 6.4: Angle of the uncertainty ellipse α with the horizontal axis of the auxiliary coordinate system used by the respective reconstruction algorithm, which may differ in its exact definition from the equator system. The similarity of the curves for Paraboloid and SegmentedSpline suggests that both use the same definition.

The size of the ellipse is not affected. In two ways can the auxiliary system deviate from the equator system: The axis definition could be swapped, and they could be defined in reverse. For given values of the orientation angles, these different axis definitions translate into different definitions of the angle: It could be measured from another axis than the horizontal one, or clockwise instead of counter-clockwise.

Both operations are applied to the angles in two analyses, which are performed twice for SplineMPE and SegmentedSpline. The results are compared to the same analysis with the unchanged angles. For SplineMPE, the original maximum significance of 6.0σ became $(5.7\sigma, 6.8\sigma)$, and SegmentedSpline changed from 6.5σ to $(5.7\sigma, 7.0\sigma)$ for (reversed, swapped) axes. For both reconstructions, the swapped axes increase the significance of the Moon shadow, which is an indication that the wrong definition for the auxiliary system was assumed.

However, one cannot change the angle orientation based on these findings alone. A more detailed study and code review of the implementation would be needed, which would have exceeded the scope of this thesis. Instead, the analyses comparing the reconstructions are carried out a second time with the alternative ellipse orientation. It should be noted that both uncertainty algorithms most likely use the same definition of the auxiliary system. This can be seen in the distribution of orientation angles in Fig. 6.4, which displays the same structure for both algorithms. The origin of this structure is not important here; however, it serves to show that Paraboloid and SegmentedSpline use the same definition of the axis orientation[2].

[2] A reversed axis could still be a difference between those algorithms, as the distribution is symmetric. However, a swap of the axes is what increased the significance here, and a swapped definition of the axes between the algorithms would be visible as a distribution shifted by 90°.

Table 6.2.: Maximum source significances for the five Moon cycles using SplineMPE reconstruction. Additionally, statistics of the five data samples are shown: *Sample events* are the number of events in the entire sample after processing and quality cuts, and *source events* are the number of events in the source window that enter into the analysis (with uncertainty cut necessary for the analysis applied).

Moon cycle	1	2	3	4	5
livetime [days]	9.7	11.3	11.2	12.4	11.7
sample events [10^6]	50.9	59.0	51.3	57.6	49.8
source events [10^6]	1.18	1.45	1.17	1.34	1.15
source significance	6.5σ	5.4σ	3.9σ	7.1σ	6.1σ

6.3. Comparison of Moon cycles

All previous tests were made with data from Moon cycle 1. Before the reconstructions are compared with each other, which will be done for several Moon cycles, the cycles themselves are compared. SplineMPE will be used as a baseline for this comparison. The maximum source significances and statistics information about the cycles is shown in Tab. 6.2, and pointing contours for the five cycles in Fig. 6.5.

Both in source significance and pointing contour, cycle 3 is visible as a clear outlier. The significance is smaller, and the 1σ-contour is distorted and much larger than for the other cycles. Even without cycle 3, the differences between cycles are large: The source significance varies by nearly 2σ and the 1σ-contours vary in size along either coordinate between 0.08° and 0.22°. Three of the five cycles can locate the Moon with a 3σ certainty inside an area about the size of the Moon. The best-fit position is shifted by maximally the Moon radius.

6.3.1. Differences between cycles

The maximum source significance of the Moon shadow increases with more data, and such it is natural to look at differences in the statistics of the cycles. Both in the number of events in the source window, as well as the entire data sample, cycle 3 is not an exception from the other cycles. The only cycle with nearly 100 % livetime is cycle 4, and this is also the most significant of the five. However, the cycle with the least amount of livetime has a relatively large significance. Livetime is not a measure for the amount of events in the cycle, because the rate varies during the Moon cycle. Thus, the exact distribution of livetime in the time of the Moon cycle is more relevant than the total

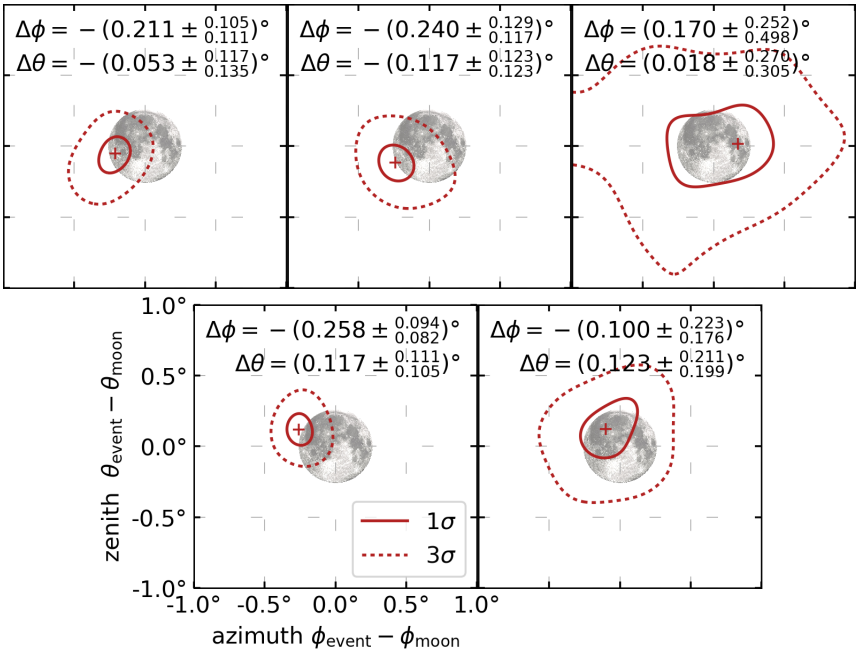

Figure 6.5.: Pointing contours for the SplineMPE reconstruction in all five cycles ($1-3$ top row, $4-5$ bottom row).

amount. In the appendix in Fig. B.1 the rate can be seen as function of time, where gaps in the livetime are visible as pieces missing in the otherwise smooth curve.

Times in a Moon cycle determine the azimuth and zenith position of the Moon, and therefore livetime gaps will not affect all zenith and azimuth values equally. For example, gaps in the middle of a cycle remove events with certain zeniths that do not occur anywhere else in the cycle. Generally, the time in the cycle is related to Moon azimuth and zenith, which is related to observables like energy. Therefore, livetime gaps can have a complex impact on several observables that are used in the analysis, and thus could cause a reduced significance for a cycle.

Apart from gaps in the livetime, the alignment of the Moon cycle with the time of day is relevant. The Moon performs approximately one revolution in azimuth each day, and a Moon cycle is not an integer number of days. Therefore, the distribution of absolute azimuth will never be flat, but will show a small step. Additionally, livetime gaps change this distribution further; it will be different for each Moon cycle, as can be seen in Fig. 6.6. This azimuth distribution affects other observables, for example due to the azimuth-dependence of the detector geometry.

In summary, there are intrinsic differences between Moon cycles that could potentially cause significances to vary substantially. Additionally, livetime gaps could increase these

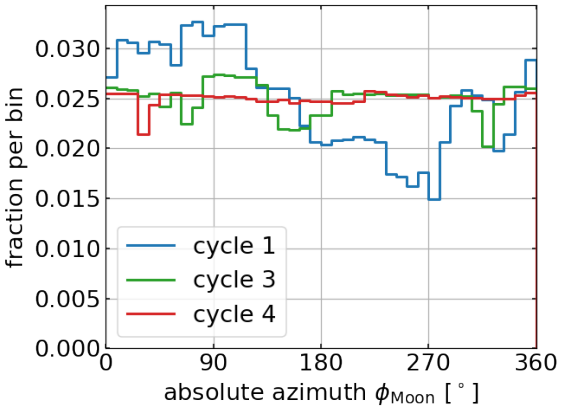

Figure 6.6: Absolute azimuth of the Moon for selected cycles. The richness in features of cycle 1 coincides with this cycle's small livetime, while cycle 4 has only a single small downtime that causes this small dip.

differences, and consequently, a cycle with large livetime would be affected less severely; although a cycle affected strongly by livetime would not necessarily have to be impacted much.

The observables that are directly used in the analysis are compared for all five cycles in Sec. B: The averaged uncertainty, uncertainty ellipse angle, energy estimator used in the pull correction and azimuth zenith. Most distributions match nearly perfectly. In Zenith, cycles 1 and 2 deviate from the other three, but no unexpected features are visible. In particular, the outlier cycle 3 does no deviate from the others.

It remains unclear, why cycle 3 has such a small significance. Possibly, it can be attributed to random fluctuations. In this case, the Moon analysis would be very sensitive, and require a larger data sample to be stable. Combining several cycles and performing the analysis with the combined data, would decrease the impact from random fluctuations.

6.3.2. Influence of geomagnetic field

The geomagnetic field is very stable on the time scales of a Moon cycle or between Moon cycles [41]. Therefore, differences between Moon cycles cannot be attributed to some geomagnetic time variability.

The shift of the most likely Moon position due to the geomagnetic field can be observed for four out of five cycles, with cycle 3 being unreliable in its estimate. The position is consistently shifted to smaller azimuths. This matches the expectation explained in Sec. 2.2.2: The approximately symmetrical alignment of IceCube with the geomagnetic dipole field causes the deflection experienced by any cosmic ray to be aligned always in the same azimuth direction as observed from IceCube's point of view. Therefore, in

relative coordinates, a shift in one defined direction is observed. The average shift of the shadow calculated from four cycles in azimuth is $-\left(0.20^{+0.07}_{-0.06}\right)^{\circ}$.

A shift in the zenith direction is also observable. This would not be expected if IceCube were positioned at the geomagnetic pole, as assumed above: The deflection direction, which is the cross product of trajectory and dipole field lines, would have only a component in azimuth direction. The real position of IceCube, which is offset by 11° in latitude from the geomagnetic pole, causes the plane that contains the trajectory and magnetic field lines to not be vertical anymore all the time. A deflection direction with a zenith component is the result.

6.4. Verification of uncertainty scaling

The pull correction that was performed in Sec. 4.3.3 has the goal to rectify systematic errors of the uncertainty estimation. As was shown already, the correction does improve the uncertainty estimations; however, it is not a perfect correction, as was shown by the application of the correction to the same data used for its calculation. Therefore, the correctness of the pull correction is tested.

This is done by scanning over different pull correction factors surrounding the found correction, and plotting the resulting significance of the analysis that is carried out with this modified data. A maximum in significance is expected at the position of the best pull correction, because at this pull correction the systematic error of the uncertainties is rectified, and thus, the analysis produces the best result.

In Fig. 6.7 the results of the pull scan are given. The x-axis gives the factor that is multiplied with the normal pull correction, which is carried out first. Therefore, all uncertainties are scaled according to the energy as usual, and the result is then scaled for all events by the given additional factor. To remove effects from different statistics on the significance, for all scan points of a cycle, the same uncertainty cut must be applied in the analysis. The largest scan factor causes the largest uncertainties; therefore, all scan points on a line use the data sample from the right-most point.

Of the five cycles, four cycles display a maximum at 1.0 or around that. Cycle 2, however, deviates substantially, and peaks at 0.6. This means, that for cycle 2 the uncertainties are nearly twice as large as they should be to match the reality nest, which should give the best Moon analysis significance. The reason for this deviation, as for the other deviations between cycles discussed in the previous section, is unclear.

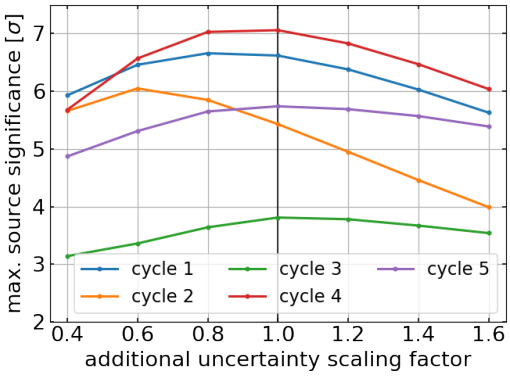

Figure 6.7: Maximum source significances for different uncertainty scaling factors: Uncertainties are multiplied by the given factor additionally after pull correction. Vertical black bar at 1.0 indicates no additional scaling. The uncertainty cuts are for all points on a line done using the largest scaling (such that each point on a line uses the same data).

7. Comparison of reconstruction algorithms

In this chapter, the SegmentedSpline and RNN reconstruction algorithms are compared to SplineMPE acting as an established baseline. First, a simple binned 1D analysis is performed in Sec. 7.1 to check that a Moon shadow is observable. Afterwards, in Sec. 7.2, the unbinned 2D analysis is performed. Simulation data is used in Sec. 7.3 for a comparison of the reconstructions with the true direction. The findings are discussed in Sec. 7.4.

7.1. Binned 1D analysis

The binned one-dimensional analysis is based on counting the number of events inside of bins, and is therefore a very fast analysis. This makes it suitable as a way to make sure that a Moon shadow is observable, before a more involved analysis is started.

Because this analysis simply compares bin contents without providing a proper background hypothesis, the event rate in the source and background windows must be equal (the shadowing of the Moon is negligible with regard to the entire window). Therefore, only data for which no background reduction was done during processing can be used, which excludes SegmentedSpline. Also Paraboloid was subject to background reduction; however, as this analysis does not use an uncertainty estimate, it can be performed with SplineMPE, as well as the RNN reconstruction.

All five Moon cycles were used for the analysis. The relative shadowing as function of the angular distance to the Moon is shown in Fig. 7.1. A clear deficit of up to about 8 % can be observed in the 1° range around the Moon that becomes a plateau at 0, indicating no shadowed events, for larger distances.

The choice of the bin size influences the result: Larger bins can lead to loss of information due to the averaging over a larger range, and smaller bins are less reliable because of the small statistics in every individual bin (see large errors for 0.2° bin width). For a bin width of 0.5°, the two bins closest to the Moon show a smaller value for the RNN reconstruction than for SplineMPE. This difference is, however, not very large, and lies within the statistical uncertainty. Overall, the statistics is not sufficient to make a

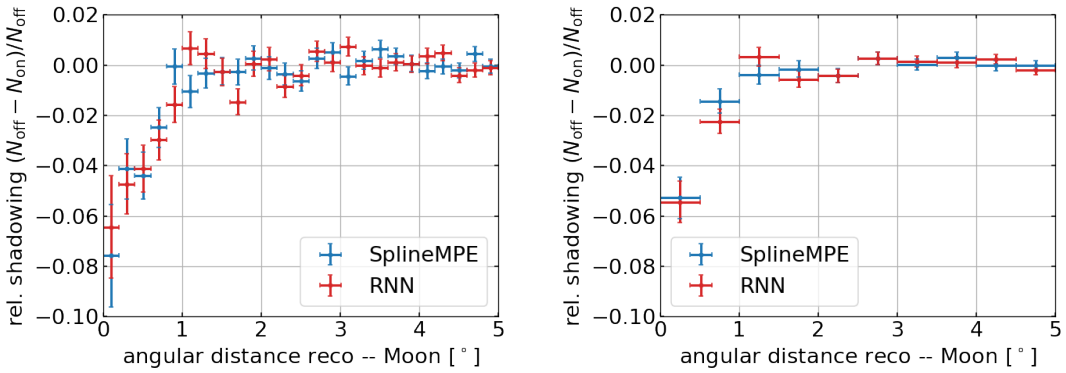

Figure 7.1.: Binned 1D analysis for five Moon cycles for two different binnings (left: bin width 0.2°, right: 0.5°). Further binnings in the appendix in Fig. A.3.

statement about which of the two reconstructions leads to a deeper Moon shadow, and thus has a better accuracy. Instead, more sophisticated methods are needed to derive a meaningful result. However, the binnd 1D analysis serves to show that a Moon shadow is present.

7.2. Unbinned 2D analysis

The unbinned two-dimensional analysis takes into account the uncertainty estimate. For the RNN reconstruction, only uncertainties symmetric in zenith and azimuth are available, while Paraboloid and SegmentedSpline have asymmetric estimates. Therefore, two sets of comparisons have to be made: Between SegmentedSpline and SplineMPE + Paraboloid with asymmetric uncertainties, and between RNN and SplineMPE + Paraboloid with symmetric uncertainties. As it was done for the pull correction, the asymmetric Paraboloid estimate is averaged according to (4.2) to a symmetric one. To test the hypothesis that the orientation of the uncertainty contour is parameterized wrong, as discussed in Sec. 6.2.2, a third comparison will be done for SegmentedSpline and SplineMPE with the alternative ellipse orientation.

It is important to note that results for SplineMPE with asymmetric uncertainties cannot be simply compared to the same reconstruction with symmetrical uncertainties. This is due to the uncertainty cut done in the analysis for the prevention of edge effects. This cut targets the semi-major axis of the ellipse, and therefore the averaging procedure increases the amount of events that survive this cut. Consequently, more events are used in the analysis for symmetric uncertainties than for the corresponding asymmetric ones, which influences the resulting significance.

Table 7.1.: Maximum source significances for all tested reconstruction algorithms for all five Moon cycles and for combined data sets (rightmost two columns). For the reconstructions using asymmetric uncertainty contours, the results for the alternative orientation of the ellipse are given as well.

Moon cycle	1	2	3	4	5	$1-3$	$1-5$
SegmentedSpline	6.5σ	3.4σ	3.5σ			7.7σ	
alt. uncertainty orientation	7.0σ	3.2σ	4.0σ			8.0σ	
SplineMPE	6.5σ	5.4σ	3.9σ	7.1σ	6.1σ	7.5σ	
alt. uncertainty orientation	7.2σ	5.9σ	4.6σ	6.7σ	6.6σ	8.6σ	
SplineMPE (sym. uncertainty)	6.5σ	5.0σ	4.0σ	6.6σ	6.6σ		14.0σ
RNN (sym. uncertainty)	5.5σ	4.0σ	3.9σ	4.8σ	6.1σ		12.1σ

The analysis is performed on each Moon cycle individually, and on a combined set of all Moon cycles. SegmentedSpline processing was done only for the first three cycles, so the first comparison is limited to cycles $1-3$, and the combined set for this comparison consists of those three cycles. For the RNN reconstruction, all five cycles are used individually and for the combined set. The maximum source significance for each analysis, used as the indicator of reconstruction accuracy, is given in Tab. 7.1.

SegmentedSpline

The two-dimensional significance landscapes are given for the comparison between SegmentedSpline and SplineMPE in Fig. 7.2. The general shape of the shadow, and the distribution of fluctuations around it, are for a given cycle similar in both reconstructions. This means that the fluctuations have their origin in the data sample, and are resolved by both reconstructions; they are not statistical fluctuations of the reconstruction.

Cycle 2 in SegmentedSpline has a substantially different landscape of source significances: While for all other cycles the largest significance is the deficit from the Moon, this cycle's Moon deficit has a smaller significance than some over-fluctuations. Even though the maximum source significance is small, there are other cycles with similarly small values, that do not exhibit such a large significance for fluctuations. Likewise, the statistics in this cycle are not unusually small, and are in fact larger than for the other cycles: For cycles 1 to 3, the source window contains 1.13×10^6, 1.38×10^6 and 1.10×10^6 events. Thus, the reason for this behavior is unclear.

In SplineMPE, cycle 2 has (from the set of five cycles) the smallest significance with the exception of cycle 3. This is not unexpected, given that, as shown in Sec. 6.4, cycle 2 had its maximum significance at a smaller uncertainty scaling than the one used for the analysis. The same could be the case for SegmentedSpline; however, due to time constraints,

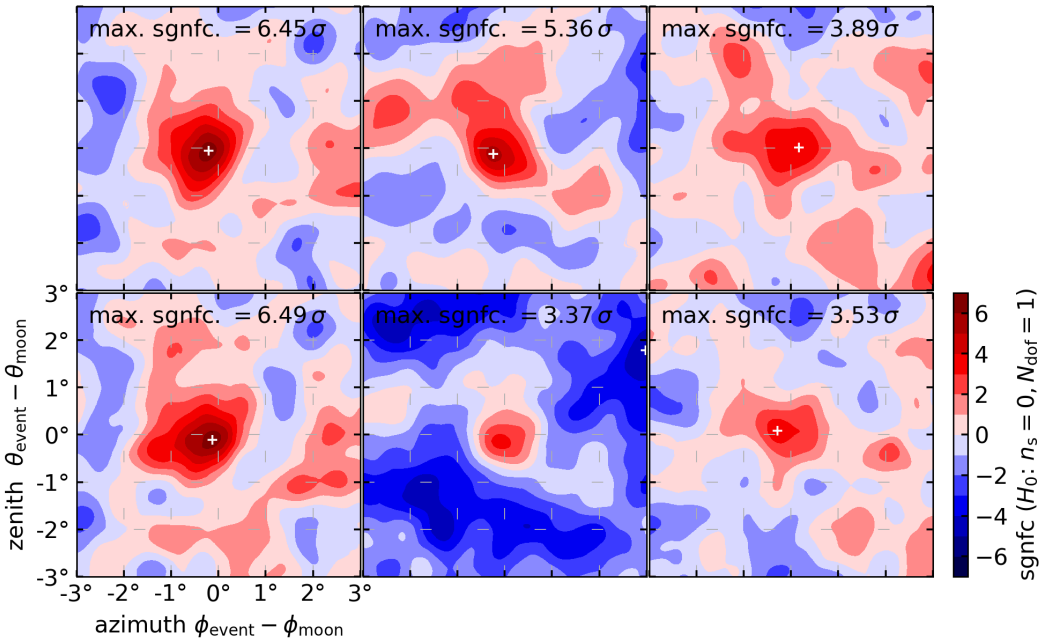

Figure 7.2.: Source significance landscapes for SplineMPE (top) and SegmentedSpline (bottom) reconstructions, for Moon cycles $1-3$ (left to right).

in this thesis no scan of the uncertainty was done for SegmentedSpline. Apart from the outlier cycle 2, the maximum source significances for SplineMPE and SegmentedSpline are similar. The largest difference is 0.4σ for cycle 3, which was identified as outlier previously in Sec. 6.3 due its small significance and non-circular pointing contour. Cycle 1 has essentially the same significance in both reconstructions.

The combined data set of the three cycles is shown in Fig. 7.3. The maximum significance for SegmentedSpline is 0.2σ larger than for SplineMPE, which is unexpected, given that SegmentedSpline performs as good or worse (but not better) than SplineMPE based on the results of individual cycles. The pointing contours are small compared to the Moon disk, with a shift in accordance to the findings in Sec. 6.3 (shift to smaller azimuths) clearly visible.

With the alternative ellipse orientation, the significances are for both reconstruction larger by 0.5σ to 0.7σ, with the exception of one cycle for SplineMPE, and the outlier cycle 2 for SegmentedSpline. If the alternative orientation would be correct[1], the comparison between the reconstructions gives for individual cycles a similar result as before. On the combined data (see in appendix in Fig. **??**), the significances are also larger than before, and are now more in line with the individual cycles: SplineMPE is

[1]Following the explanation in Sec. 6.2.2, the alternative orientation is true either for none, or for both reconstructions, but never for one, but not the other.

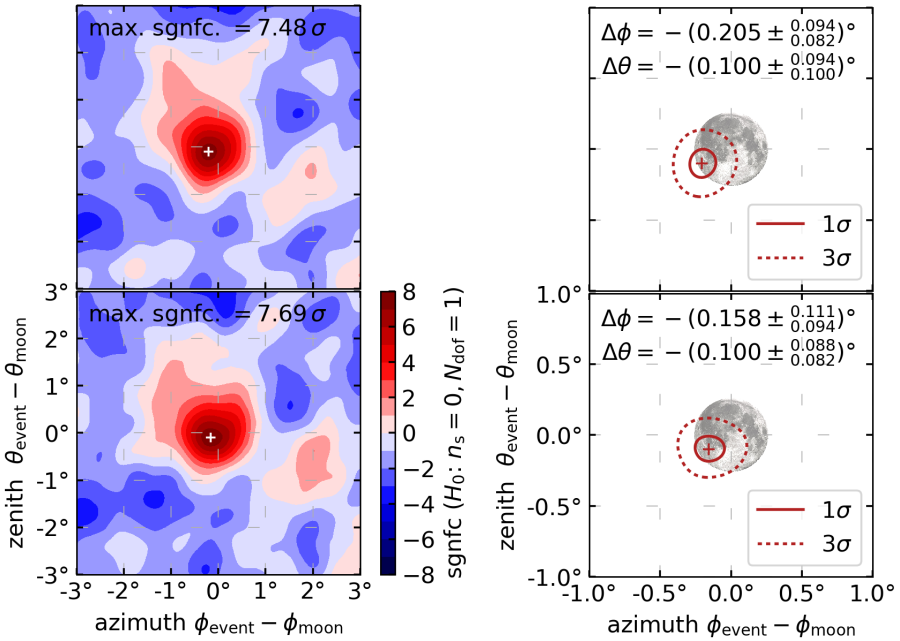

Figure 7.3.: Source significance landscape and pointing contours for SplineMPE (top) and SegmentedSpline (bottom) reconstructions with combined data from cycles 1 – 3.

more significant than SegmentedSpline by the same margin as the individual cycles. In summary, the alternative orientation is more significant, as well as better self-consistent, than the assumed orientation.

RNN reconstruction

Among the five cycles available to the RNN reconstruction, there is no such outlier as cycle 2 for SegmentedSpline. The landscape plots are shown in the appendix in Fig. A.5. The comparison with SplineMPE is simpler than before: Throughout the five cycles, SplineMPE is more significant by 0.5σ to 1.0σ, with the exception of cycle 3, where the significance is nearly the same. The combined data set has very large significances compared to the individual ones, which is expected for an analysis with five times as much data. The comparison between reconstructions is similarly clear as it was on the individual cycles with a difference of 1.9σ in SplineMPE's favor.

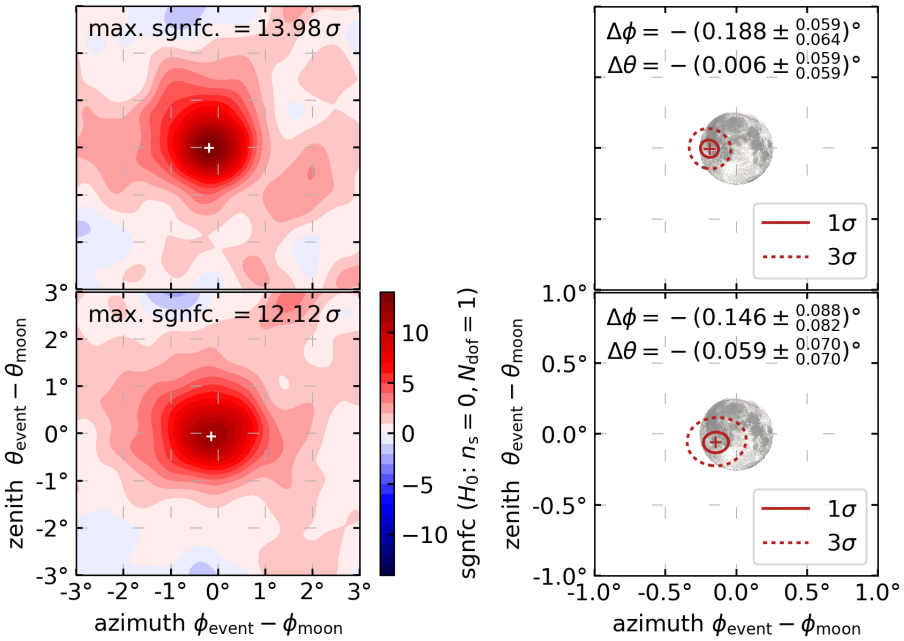

Figure 7.4.: Source significance landscape and pointing contours for SplineMPE (top) and RNN reconstruction (bottom) with combined data from cycles $1-5$ and symmetrical uncertainty contours.

7.3. True error from simulations

Optimally, enough simulation data would be available to be able to perform the Moon analysis in the same way as with experimental data. This would constitute a powerful test of the Monte Carlo simulation's match with reality. Unfortunately, the simulation data spans a livetime of about one hour, which is not sufficient for this Moon analysis. Instead, the true error is calculated as the angular distance from the Monte Carlo truth contained in the simulation data and the reconstruction. This is the traditional method of testing the accuracy of directional reconstruction algorithms.

This method also has the advantage that the reconstruction accuracy can be investigated as function of energy. A correlation between energy and error is expected, because higher-energy events produce a larger signal in the detector, which gives more information to the reconstruction algorithms. With the Moon analysis, an energy-dependent analysis is only possible for a very limited energy range, due to the strong energy-dependence of the cosmic ray flux. A comparison with the Monte Carlo truth, however, is still possible even for single events.

Table 7.2.: Median and quantiles of true error from simulations for the three reconstruction.

	10 % quantile	median	90 % quantile
SplineMPE	0.30°	1.35°	6.92°
SegmentedSpline	0.32°	1.39°	6.97°
RNN	0.35°	1.27°	5.26°

For a simple comparison of the reconstructions, the median true error with the 10 % and 90 % quantiles is calculated and shown in Tab. 7.2. The RNN reconstruction has the smallest error and also the smallest spread of the error distribution. SplineMPE has a larger error, followed by SegmentedSpline.

For the energy-dependent error, the question of which observable to use for the energy is not trivial. As opposed to single muons that originate from neutrinos and that have a defined energy, the Moon data sample consists of muon bundles from air showers. Only about 47 % of the data sample consists of muons with no other muons, or ones with negligible energy, in the bundle. For the rest, two observables could be used: The sum of all muons in the bundle, or the energy of the highest-energy muon (the "leading" muon) in the bundle. Both become the same for a single muon in a bundle. It was found that as a function of the summed muon energy, the error increases with increasing energy, which is unexpected. Contrary, the leading muon's energy shows the expected drop of the error for higher energies, and thus, the energy of the leading muon is used here. The median error per bin as function of the leading muon's energy is shown for all three reconstructions in Fig. 7.5 (top left). The relative scale of the differences between reconstruction can be seen in Fig. 7.6 (left). The displayed energy range is the entire range available in the data.

In the relative view, it is easily visible that the reconstructions' order in accuracy, as it was seen in Tab. 7.2, consists across the entire available energy range. SplineMPE has a slightly smaller error than SegmentedSpline, which deviate less than 0.05°, except for the highest-energy bin. The RNN reconstruction is better than SplineMPE throughout, and for smaller energies the error is even up to 0.2° smaller than SplineMPE.

Additionally to an energy dependency, simulations allow investigations dependent on the cosmic ray charge. The composition of the cosmic ray flux depends on the energy, and therefore, the data is additionally shown for the two composition extrema of only protons and only iron nuclei. At very high energies of the cosmic ray flux, the portion of iron can match or exceed the portion of protons (see Sec. 2.2). However, as the distribution in Fig. 7.5 (top right) shows, iron events are the minority also for the highest energies in the sample. Therefore, the median error is determined primarily by the proton population.

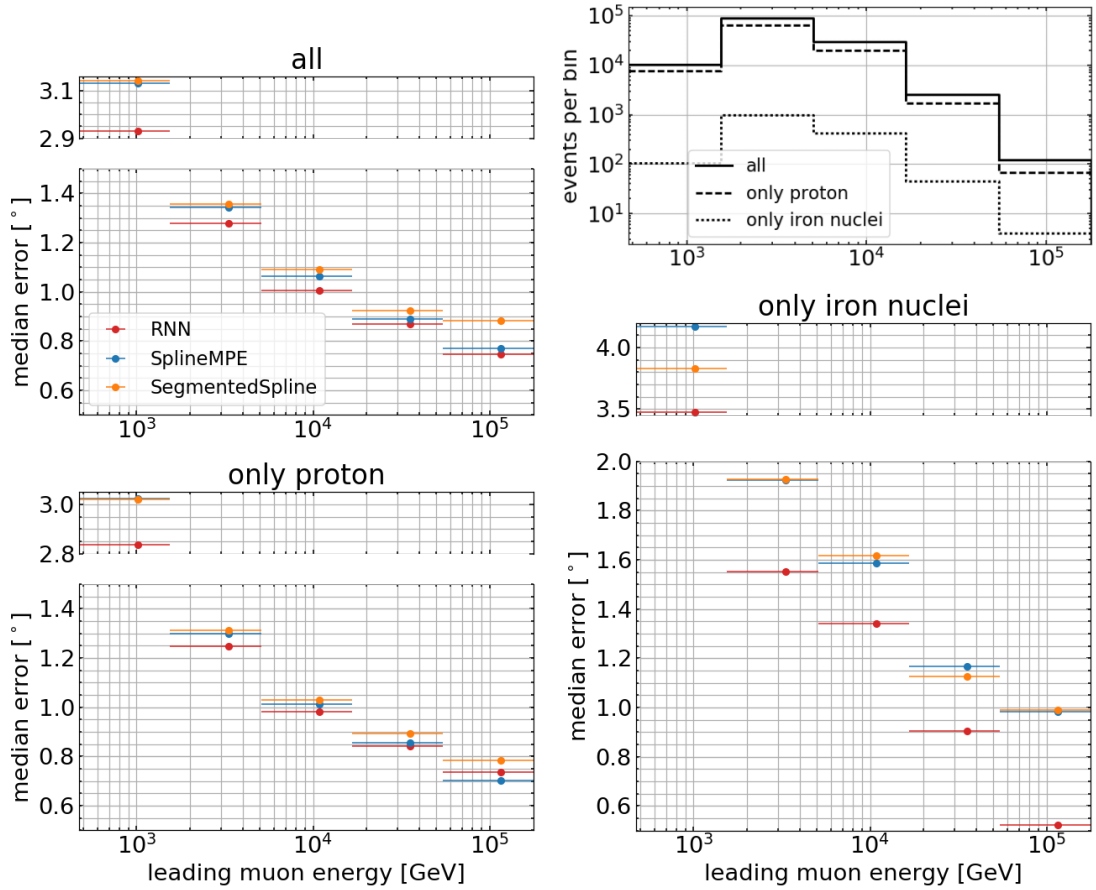

Figure 7.5.: Error from Monte Carlo truth as function of energy of the leading muon in the muon bundle. Shown is the median error for each energy bin. Top left panel uses all events, while bottom panels show only events originating from proton or iron nuclei cosmic rays. Top right panel shows the number of events in each bin.

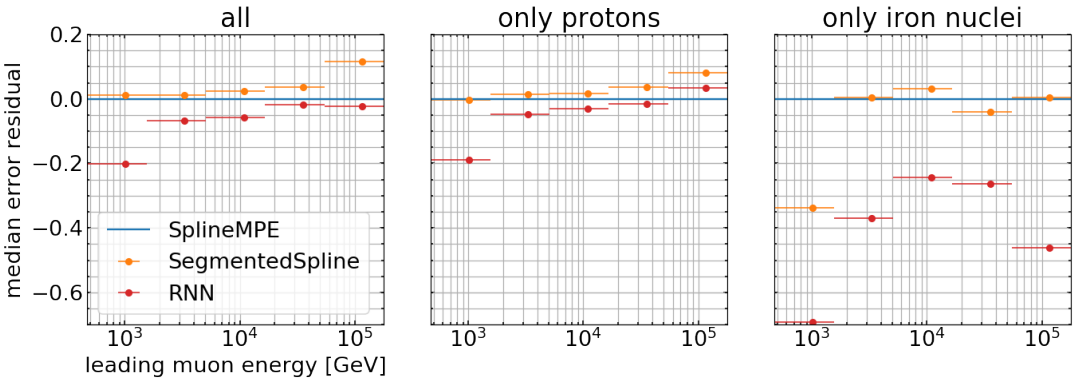

Figure 7.6.: Median error from Monte Carlo truth as function of leading muon energy, displayed as residual from the median error of the SplineMPE reconstruction.

7.4. Discussion

The combination of several Moon cycles into one large data set for the analysis has the potential to summarize this thesis by stating only few numbers. However, this procedure has the drawback, that it is unclear what difference in significances between reconstructions constitutes a significant finding: SegmentedSpline and SplineMPE differ in the combined data set by 0.2σ, but it is not clear whether this is a fluctuation or a finding. Comparing several individual Moon cycles has the advantage of providing more information: The RNN reconstruction has a smaller significance for all five Moon cycles than SplineMPE, which is unlikely to be a random fluctuation.

On the other hand, the combination of Moon cycles has the potential to average-out gaps from detector downtime in the livetime distributions of the cycles. As proposed in Sec. 6.3, livetime gaps could be responsible for cycles (like cycle 3) having a lower significance than others, even though the amount of events used in the analysis is comparable. This could explain why for SegmentedSpline, a combined result with higher significance than SplineMPE was found, even though in individual cycles SplineMPE was just as or more significant.

Overall, the comparison of SegmentedSpline and SplineMPE points towards a similar accuracy, but this result is relatively uncertain. If cycles 4 and 5 could have been processed for SegmentedSpline as well, a clearer result could be achieved, as it is the case for the RNN reconstruction. There, the accuracy of SplineMPE is clearly superior to the RNN reconstruction.

According to Monte Carlo simulations, this result is the other way around: The RNN reconstruction performs better than SplineMPE. For SegmentedSpline, simulations agree with a similar performance to SplineMPE. The reason for this mismatch between simulation and experimental data is unclear. One known discrepancy is the exclusion of coincident events from the simulation data, as described in Sec. 4.2. However, no detail into how this discrepancy could alter the true errors like observed were explored.

It is important to note, that these results are mainly valid for muon energies between about 1×10^3 GeV and 1×10^4 GeV, which is the main energy range of atmospheric muons in the Moon filter sample. This is not the entire muon energy range of interest in IceCube, and thus, the performance of the reconstructions as they are found here could be very different for higher or lower energies. Additionally, Moon data contains muon bundles instead of single muons, as it would be the case for muon-neutrinos. This may influence the RNN reconstruction in particular, as it was trained on single muon events.

8. Summary and outlook

In this thesis, for the first time, the new SegmentedSpline and RNN-based directional reconstruction algorithms were applied to a large data sample of five and three Moon cycles, respectively. These contain on the order of 50×10^6 atmospheric muon bundle events. Monte Carlo simulations of atmospheric muon bundles with about 2×10^5 events were processed. Distributions of the reconstructed events were compared with those from the best-performing standard reconstruction, SplineMPE. To quantify the accuracy of the reconstructions, a Moon shadow analysis was performed: Both a simpler, one-dimensional binned analysis, and a more sophisticated, unbinned two-dimensional analysis were used. The previously developed two-dimensional analysis is based on a maximum likelihood method that is applied on a grid, and uses a disk-shaped source hypothesis and asymmetric uncertainty estimates. The analysis was slightly modified for this thesis to include a proper coordinate system, and used with better-established methods for background determination and uncertainty scaling.

The maximum source significance derived from the analysis result was used as a measure of reconstruction accuracy in the following investigations. The optional setting of an additional continuous muon energy loss in the SegmentedSpline reconstruction was tested and was found to improve the accuracy. The exact parameterization of asymmetric uncertainties as ellipses that is used by the reconstruction algorithms was investigated, and indicates that the ellipse orientation of Paraboloid, the uncertainty estimator used with SplineMPE, is calculated wrongly. The most likely correct calculation results in swapped coordinate axes compared to the currently calculated ellipse. In most analyses, the symmetric averaged uncertainty is used, and therefore the orientation is irrelevant, which is why this error kept being unnoticed so far. As the Moon analysis used here makes use of the asymmetric uncertainties, most results are given with the alternative ellipse orientation as well.

It was found that the analysis results from different Moon cycles vary substantially, and thus the differences between the cycles were investigated. Distributions of various observables that are relevant for the analysis did not reveal any unexpected deviations between the cycles. Effects from the geomagnetic field were ruled out, and its influence on the observed shift of the shadow explained. An investigation into the correctness of the uncertainty scaling showed that for one cycle, the applied scaling did not produce the most significant Moon shadow, which is unexpected. No reason was found for the differences between Moon cycles; however, it was proposed that the varying livetime

distributions between cycles can cause the observed differences in significance of the Moon shadow.

Eventually, the reconstruction algorithms were compared based on the same data, both for individual cycles and for data from several cycles combined. All reconstructions have a good enough accuracy to clearly observe a Moon shadow. With a maximum source significance on a combined data sample of three Moon cycles of 7.5σ for SplineMPE and 7.7σ for SegmentedSpline, these reconstructions perform similarly. On all five Moon cycles (and with symmetric uncertainties, thus not directly comparable to the other result), the significances for SplineMPE and the RNN reconstruction differ more with 14.0σ and 12.1σ, respectively. This indicates that the RNN reconstruction has a slightly lower accuracy than SplineMPE. However, the meaning of these results are limited to muons with energies around 10 TeV, and thus, cannot be generalized to the entire energy range in which IceCube searches for astrophysical neutrinos. Also, the Moon data used here consists of muon bundles, and the RNN has been trained on single muons.

The results from the Moon analysis were compared with the true error of a reconstructed event, as derived from simulation data. SegmentedSpline has a slightly larger median true error than SplineMPE, which again has a larger error than the RNN reconstruction. This is the opposite from the Moon shadow result. However, it had to be assumed that the muon bundle multiplicity is negligible, which could explain the mismatch.

In conclusion, on the energy range that a Moon analysis can work with, the RNN reconstruction has a lower accuracy than SplineMPE, and SplineMPE and SegmentedSpline seem to have similar accuracy. Regarding the first statement, an RNN trained on single muons might have difficulty generalizing to muon bundles. Processing more Moon cycles with the SegmentedSpline reconstruction would allow for a clearer conclusion regarding the second statement, as only three Moon cycles were used in the comparison, and one of them behaved oddly compared to the others. Due to time constraints this was not possible to do for this thesis.

Outlook

It is possible to classify atmospheric muon events according to their primary cosmic ray charge, which can be done with a neural network trained with simulation data [42]. With such a classifier, a subset of the Moon data sample containing only proton events could be created, which all experience the same (energy-dependent) deflection in the geomagnetic field. This is opposed to the situation in the full sample, where a range of different cosmic ray primaries cause many different deflection strengths. Thus, with a pure proton sample, the Moon shadow would be only slightly smeared out, and a Moon analysis on this data sample could give a more significant result.

Alternatively, it would be possible to perform a Moon analysis using only events from iron nuclei, in order to investigate the geomagnetic field itself. Iron nuclei experience a stronger deflection, and thus a better observable geomagnetic shift of the Moon shadow. At the same time, iron events are more energetic, which causes a smaller shift; however, these effects will most likely not cancel out completely.

For a pure iron sample, large amounts of data would be needed, because the portion of iron events in the Moon filter is only about 1 %. Thus, to observe a Moon shadow with similar significance as a full data sample, about 100 times the data is necessary. From the results in this thesis it is clear that one Moon cycle of data is sufficient to observe a significant shadow in most cases. Thus, one would need to combine at most 100 Moon cycles of data for an iron-dominated Moon analysis. In principle, this much Moon filter data is available.

A. Additional plots

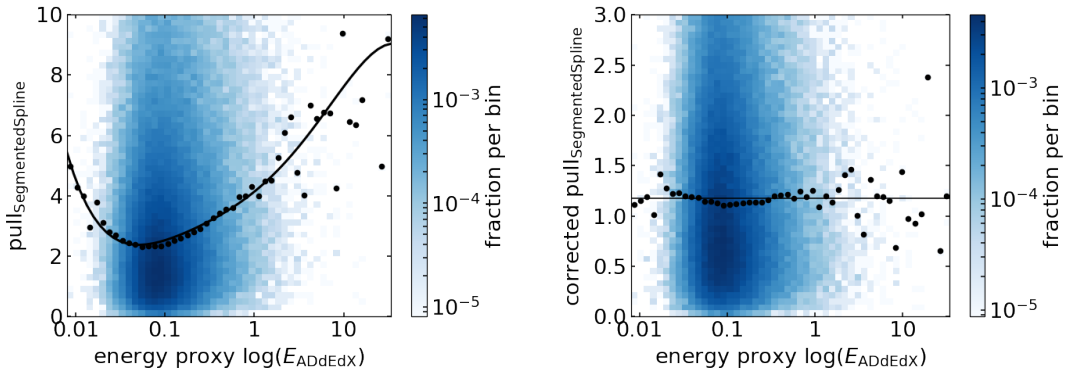

Figure A.1.: Distribution of pull and energy proxy ADdEdX for the SegmentedSpline uncertainty estimator.

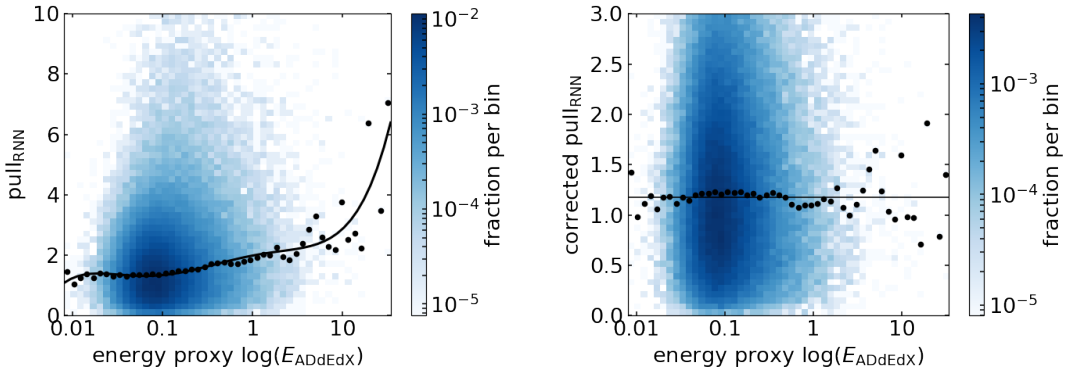

Figure A.2.: Distribution of pull and energy proxy ADdEdX for the RNN uncertainty estimator.

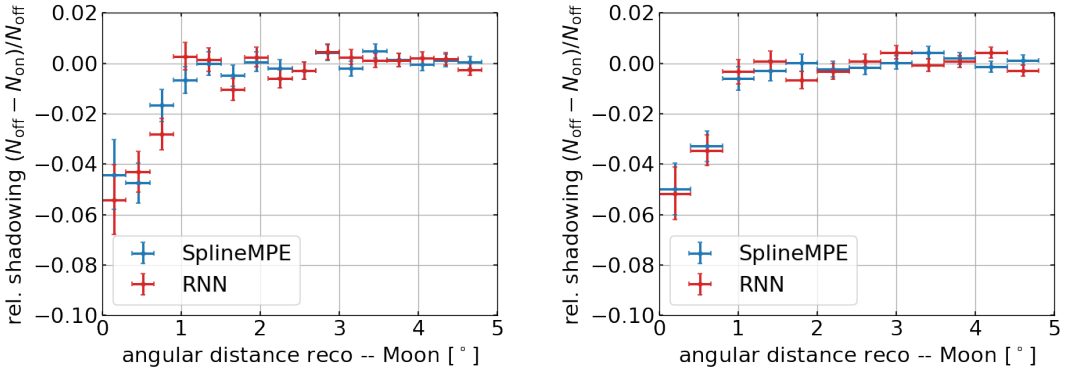

Figure A.3.: Binned 1D analysis for five Moon cycles for two additional binnings (left: bin width 0.3°, right: 0.4°). Original: Fig. 7.1.

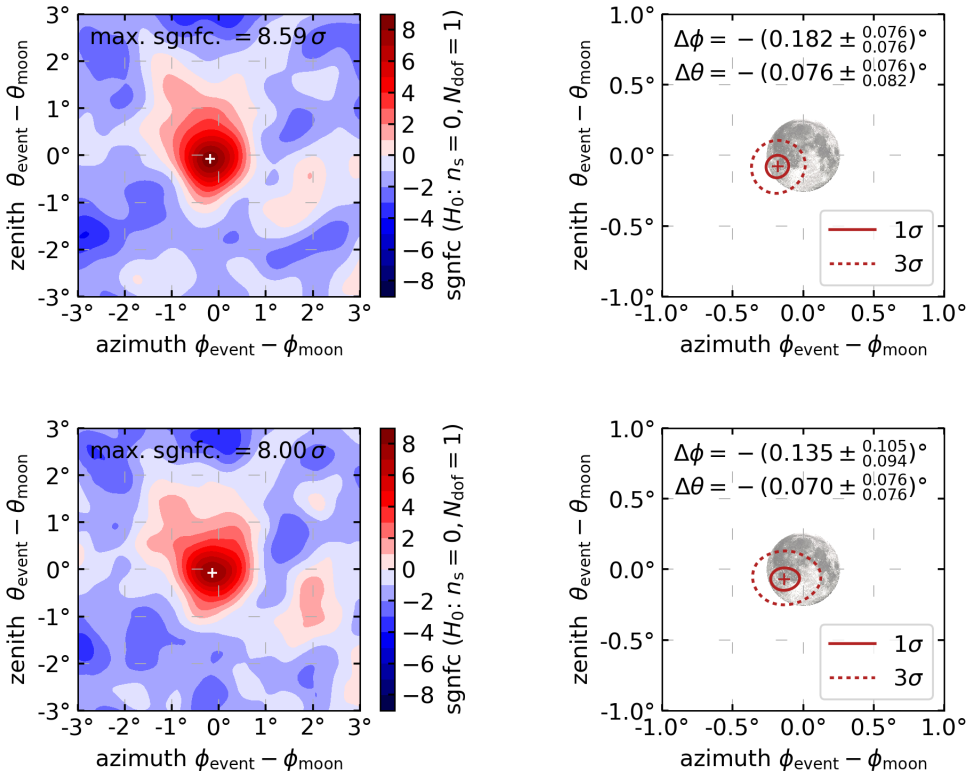

Figure A.4.: Source significance landscape and pointing contours for SplineMPE (top) and SegmentedSpline (bottom) reconstructions with combined data from cycles $1-3$, with the alternative ellipse orientation.

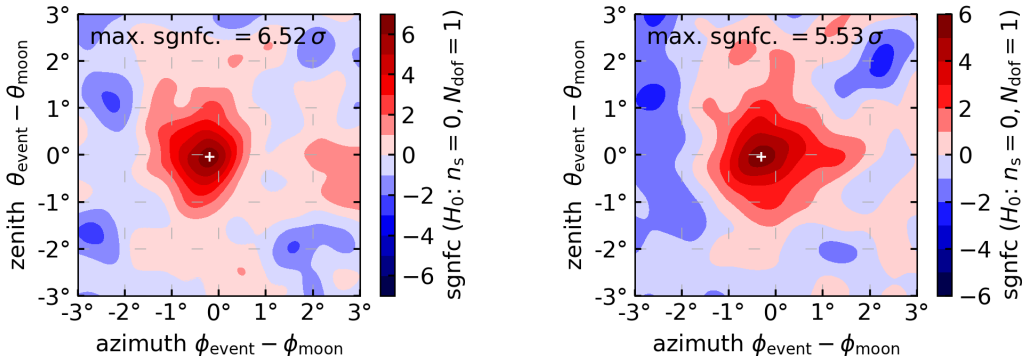

Figure A.5.: Source significance landscape for SplineMPE (left) and RNN reconstruction (right) for cycle 1.

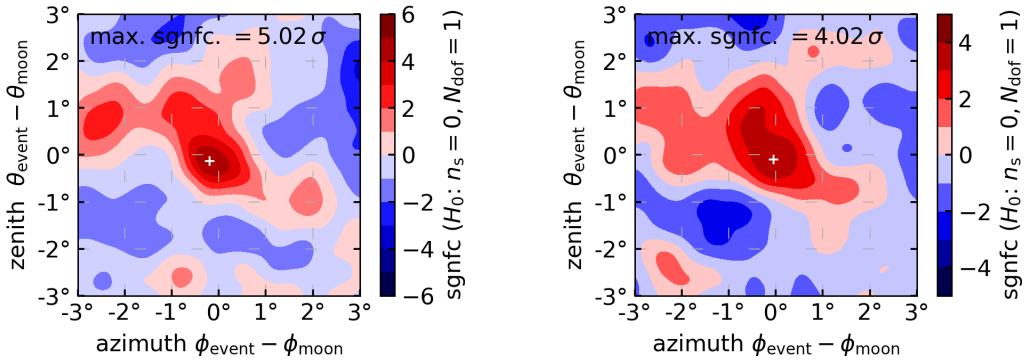

Figure A.6.: Source significance landscape for SplineMPE (left) and RNN reconstruction (right) for cycle 2.

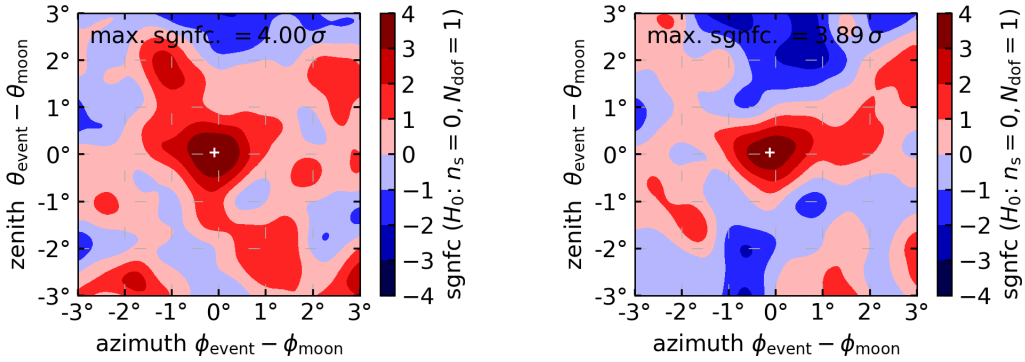

Figure A.7.: Source significance landscape for SplineMPE (left) and RNN reconstruction (right) for cycle 3.

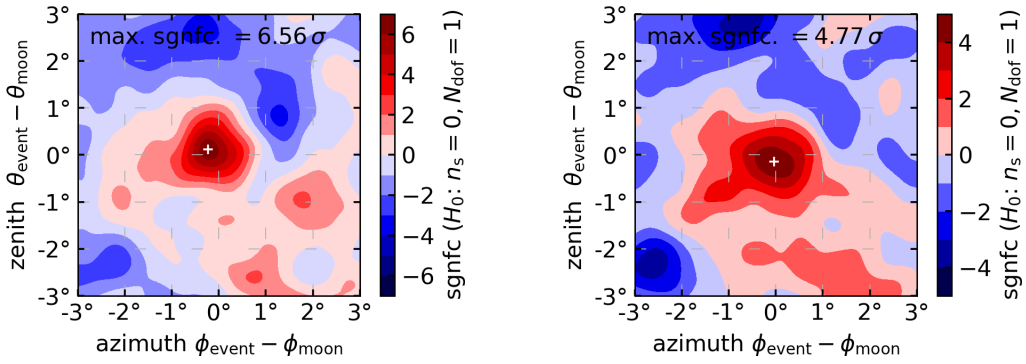

Figure A.8.: Source significance landscape for SplineMPE (left) and RNN reconstruction (right) for cycle 4.

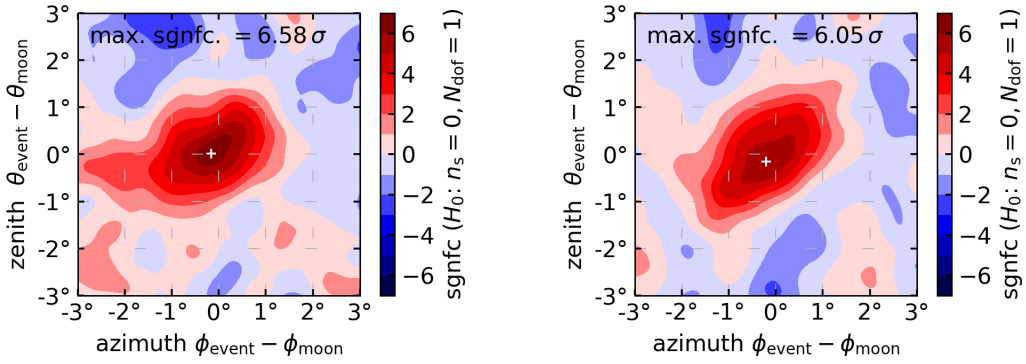

Figure A.9.: Source significance landscape for SplineMPE (left) and RNN reconstruction (right) for cycle 5.

B. Comparison of Moon cycles

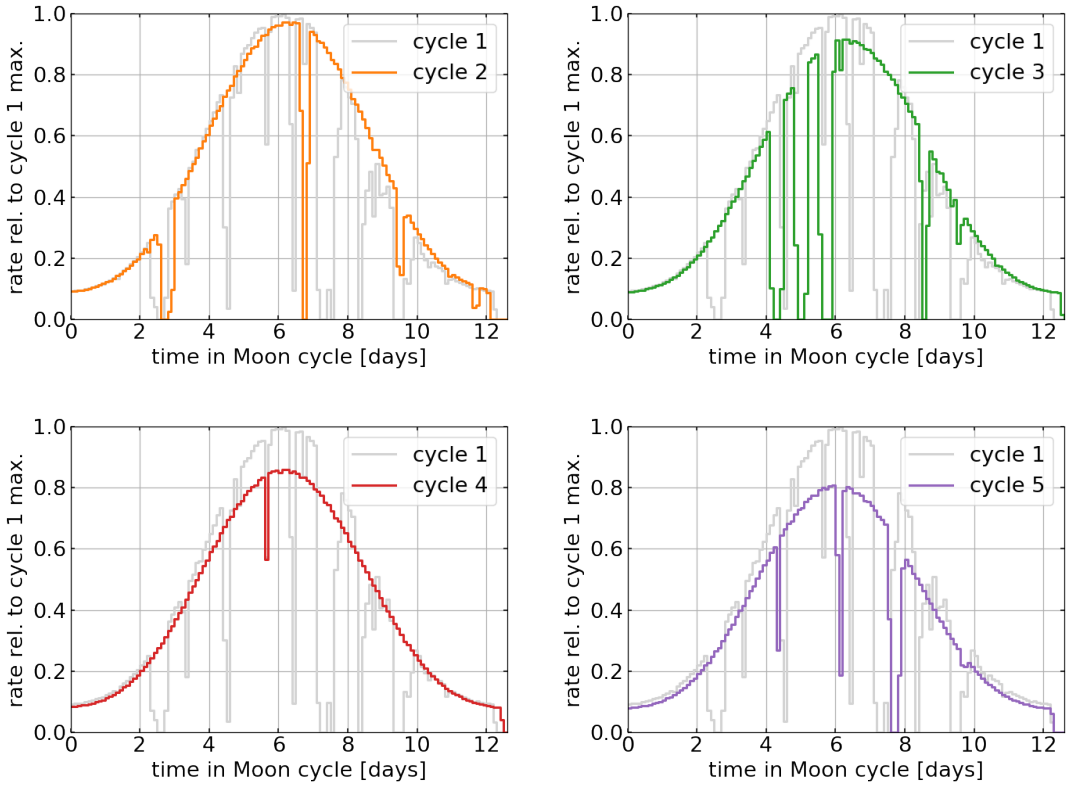

Figure B.1.: Rate as function of time in the Moon cycles $2-4$, shown relative to the rate in cycle 1.

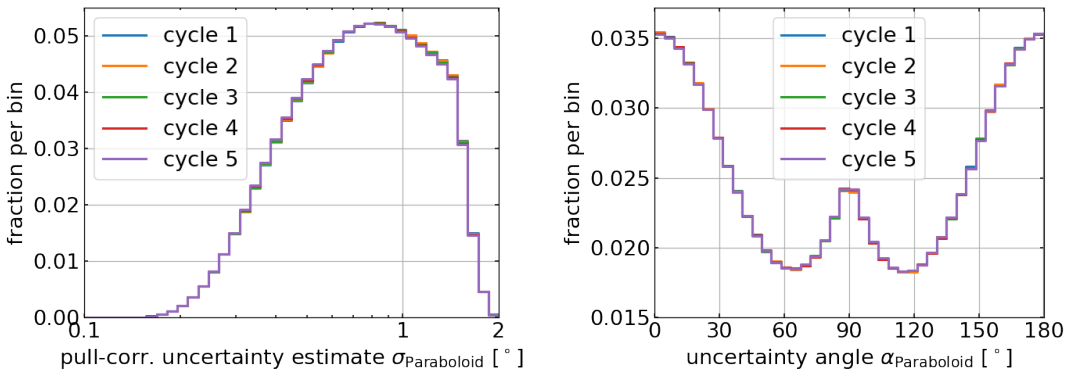

Figure B.2.: Uncertainty and ellipse angle for cycles $1-5$.

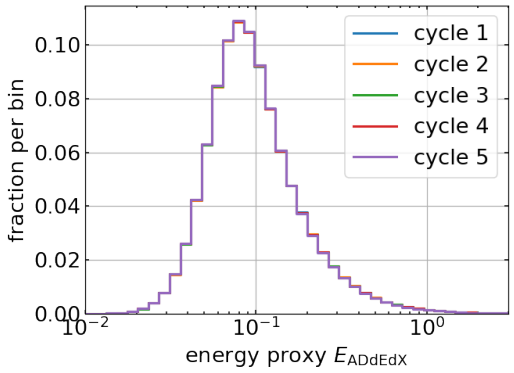

Figure B.3: Energy estimator for cycles $1-5$.

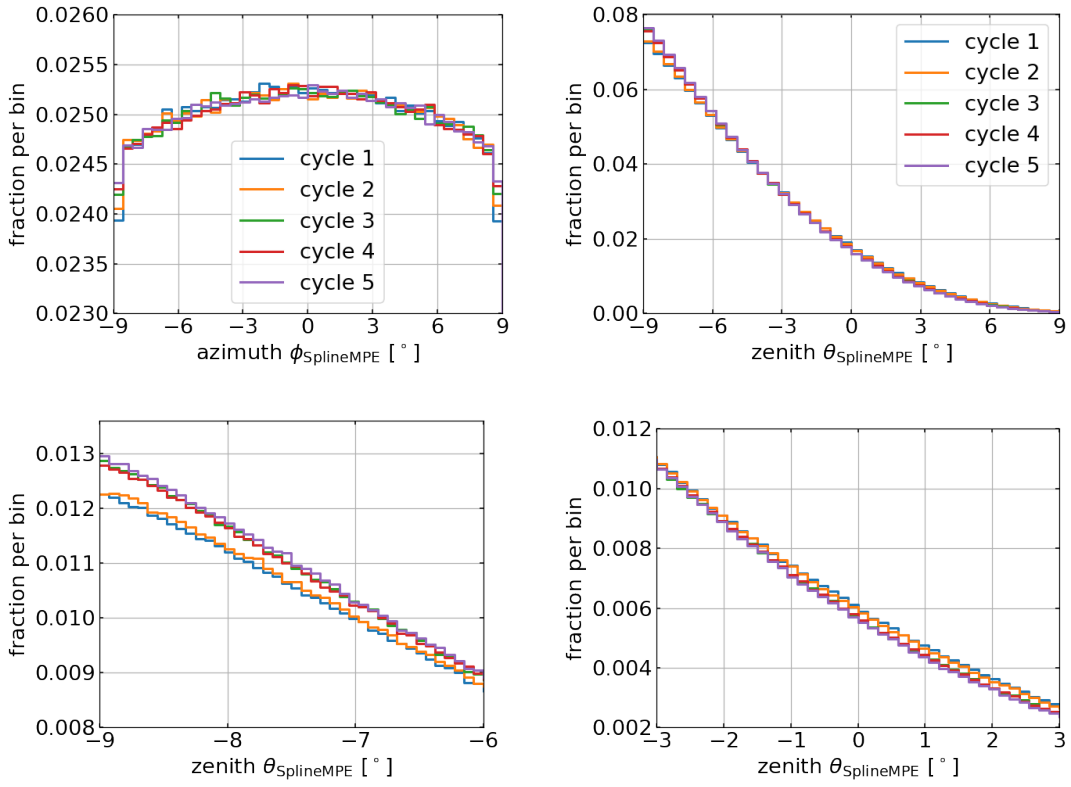

Figure B.4.: Azimuth and zenith in equator system for cycles $1-5$.

Bibliography

[1] *Moon and Sun shadowing effect in the MACRO detector*, MACRO Collaboration (M. Ambrosio et al.), Astroparticle Physics 20, 2 (2003), DOI: 10.1016/S0927-6505(03)00169-5.

[2] *The Crab Nebula as a standard candle in very high-energy astrophysics*, M. Meyer, D. Horns, H.-S. Zechlin, Astronomy and Astrophysics 523 (2010), DOI: 10.1051/0004-6361/201014108.

[3] *Recurrent Neural Networks for Reconstructing Muons*, G. Wrede, IceCube-internal telephone conference (2020).

[4] *Wikimedia Commons - File:Standard Model of Elementary Particles.svg*, Website `https://commons.wikimedia.org/wiki/File:Standard_Model_of_Elementary_Particles.svg`, accessed on 26/10/2020.

[5] *Review of Particle Physics*, P.A. Zyla et al. (Particle Data Group), Progress of Theoretical and Experimental Physics, Vol. 2020, 8 (2020), DOI: 10.1093/ptep/ptaa104

[6] *Sensitivity of the IceCube detector to astrophysical sources of high energy muon neutrinos*, IceCube Collaboration, Astroparticle Physics 20, 5 (2004), DOI: 10.1016/j.astropartphys.2003.09.003.

[7] *Evidence for High-Energy Extraterrestrial Neutrinos at the IceCube Detector*, IceCube Collaboration, Science 342 (2013), DOI: 10.1126/science.1242856.

[8] *Multimessenger observations of a flaring blazar coincident with high-energy neutrino IceCube-170922A*, The IceCube, Fermi-LAT, MAGIC, AGILE, ASAS-SN, HAWC, H.E.S.S, INTEGRAL, Kanata, Kiso, Kapteyn, Liverpool telescope, Subaru, Swift/NuSTAR, VERITAS, and VLA/17B-403 teams, Science 361 (2018), DOI: 10.1126/science.aat1378.

[9] *Flux of Atmospheric Neutrinos*, T. K. Gaisser and M. Honda, Annual Review of Nuclear and Particle Science 52 (2002), DOI: 10.1146/annurev.nucl.52.050102.090645.

[10] *The neutrino emission of SN1987A*, R. Schaeffer, Y. Declais, S. Jullian, Nature 330

(1987), DOI: 10.1038/330142a0.

[11] *The T2K Experiment - Neutrino Detection*, Website `https://t2k-experiment.org/neutrinos/neutrino-detection/`, accessed on 27/10/2020.

[12] *Measuring the neutrino mass hierarchy with the future KM3NeT/ORCA detector*, J. Hofestädt, Ph.D. thesis, University of Erlangen-Nürnberg, 2017.

[13] *IceCube - Research Highlights*, Website `https://icecube.wisc.edu/science/highlights/`, accessed on 29/10/2020.

[14] *Wikimedia Commons - File:Cosmic ray flux versus particle energy.svg*, Website `https://commons.wikimedia.org/wiki/File:Cosmic_ray_flux_versus_particle_energy.svg`, accessed on 12/09/2019.

[15] *Observation of the Cosmic-Ray Shadow of the Moon with IceCube*, IceCube Collaboration, Physical Review D 89, 10 (2014), DOI: 10.1103/PhysRevD.89.102004.

[16] *NASA - Cosmic Rays*, Website `https://imagine.gsfc.nasa.gov/science/toolbox/cosmic_rays1.html`, accessed on 29/10/2020.

[17] *A three-dimensional self-consistent computer simulation of a geomagnetic field reversal*, G. A. Glatzmaiers, P. H. Roberts, Nature 377, 203 (1995), DOI: 10.1038/377203a0.

[18] *HyperPhysics - Magnetic Field of the Earth*, Website `http://hyperphysics.phy-astr.gsu.edu/hbase/magnetic/MagEarth.html`, accessed on 30/10/2020.

[19] *The Alpha Magnetic Spectrometer on the International Space Station*, A. Kounine, International Journal of Modern Physics E 21, 8 (2012), DOI: 10.1142/S0218301312300056.

[20] *Cosmic Rays*, J. G. Wilson, G. E. Perry, Crane Russak and Co. (1976), ISBN: 978-0-844-81167-3.

[21] *Wikimedia Commons - File:AirShower.svg*, Website `https://commons.wikimedia.org/wiki/File:AirShower.svg`, accessed on 13/09/2019.

[22] *Muon Stopping Power and Range Tables 10 MeV – 100 TeV*, D. E. Groom, N. V. Mokhov, S. I. Striganov, Atomic Data and Nuclear Data Tables 78, 2 (2001), DOI: 10.1006/adnd.2001.0861.

[23] *Detektoren für Teilchen und Strahlung 1* (Particle and Radiation Detectors 1), A.

Lehmann, lecture slides, University of Erlangen-Nürnberg, 2018.

[24] *Teilchendetektoren* (Particle Detectors), H. Kolanoski, N. Wermes, Springer (2016), ISBN: 978-3-662-45350-6.

[25] *The IceCube Neutrino Observatory: Instrumentation and Online Systems*, IceCube Collaboration, Journal of Instrumentation 12 (2017), DOI: 10.1088/1748-0221/12/03/P03012.

[26] *IceCube Masterclass*, Website `https://masterclass.icecube.wisc.edu/`, accessed on 01/11/2020.

[27] *Encyclopedia of Astronomy and Astrophysics*, R. A. Meyers and S. N. Shore, Academic Press (1989), ISBN: 978-0-122-26690-4.

[28] *Observations of the Moon Shadow in Cosmic-Ray-Induced Muons with the IceCube Neutrino Observatory*, S. Philippen, M.Sc. thesis, RWTH Aachen University, 2019.

[29] *Time-Integrated Searches for Point-like Sources of Neutrinos with the 40-String IceCube*, IceCube Collaboration, Astrophysical Journal 732 (2011), DOI: 10.1088/0004-637X/732/1/18.

[30] *CORSIKA: a Monte Carlo code to simulate extensive air showers*, D. Heck, J. Knapp, J. N. Capdevielle, G. Schatz, T. Thouw, Forschungszentrum Karlsruhe Report FZKA 6019 (1998), `https://www.iap.kit.edu/corsika/70.php`.

[31] *On the knee in the energy spectrum of cosmic rays*, J. R. Hörandel, Astroparticle Physics 19, 2 (2003), DOI: 10.1016/S0927-6505(02)00198-6.

[32] *Estimating the angular resolution of tracks in neutrino telescopes based on a likelihood analysis*, T. Neunhöffer, Astroparticle Physics 25, 3 (2006), DOI: 10.1016/j.astropartphys.2006.01.002.

[33] *Muon track reconstruction and data selection techniques in AMANDA*, AMANDA Collaboration, Nuclear Instruments and Methods in Physics Research Section A: Accelerators, Spectrometers, Detectors and Associated Equipment 524, 1-3 (2004), DOI: 10.1016/j.nima.2004.01.065.

[34] *An improved muon track reconstruction for IceCube*, F. Bradascio, T. Glüsenkamp, Proceedings of Science ICRC2019 (2019), DOI: 10.22323/1.358.0846.

[35] *Detection of the Temporal Variation of the Sun's Cosmic Ray Shadow with the IceCube Detector*, IceCube Collaboration, Astrophysical Journal 872, 2 (2019), DOI:

10.3847/1538-4357/aaffd1.

[36] *Methods for point source analysis in high energy neutrino telescopes*, J. Braun, J. Dumm, F. De Palma, C. Finley, A. Karle, T. Montaruli, Astroparticle Physics 29, 4 (2008), DOI: 10.1016/j.astropartphys.2008.02.007.

[37] *The Large-Sample Distribution of the Likelihood Ratio for Testing Composite Hypotheses*, S. S. Wilks, Annals of Mathematical Statistics 9, 1 (1938), DOI: 10.1214/aoms/1177732360.

[38] *Untersuchungen mit Graphik-Prozessoren (GPU) zur Messung der Abschattung kosmischer Strahlung durch den Mond in IceCube* (Invesigations using Graphics Processing Units (GPU) of the Shadowing of cosmic rays by the Moon in IceCube), R. Reimann, B.Sc. thesis, RWTH Aachen University, 2011.

[39] *GPUs in experimental particle physics*, N. Berger, American Physical Society April Meeting 2012, abstract ID: BAPS.2012.APR.B5.3.

[40] *Time and Date - Moon distances for South Pole, Antarctica in year 2013*, Website `https://www.timeanddate.com/astronomy/moon/distance.html?year=2013&n=468`, accessed on 23/11/2020.

[41] J. Tjus, Personal communication, 2020

[42] *Klassifikation kosmischer Strahlung im Rahmen des IceCube Projekts mittels neuronaler Netze* (Classification of Cosmic Rays using Neural Networks with the IceCube Project), J. Bartl, B.Sc. thesis, Friedrich-Alexander-Universität Erlangen-Nürnberg, 2019.

Statutory Declaration

I declare that I have developed and written the enclosed Master's Thesis completely by myself, and have not used sources or means without declaration in the text. Any thoughts from others or literal quotations are clearly marked. The Master's Thesis was not used in the same or in a similar version to achieve an academic grading, or is being published elsewhere.

Place, Date	Sebastian Schindler